

# Atomic Modulation and Structure Design of Carbons for Bifunctional Electrocatalysis in Metal–Air Batteries

Yiyin Huang, Yueqing Wang, Cheng Tang, Jun Wang, Qiang Zhang,\* Yaobing Wang,\* and Jintao Zhang\*

With the extensive research and development of renewable energy technologies, there is an increasing interest in developing metal-free carbons as a new class of bifunctional electrocatalysts for boosting the performance of metal–air batteries. Along with significant understanding of the electrocatalytic nature and the rapid development of techniques, the activities of carbon electrocatalysts are well-tailored by introducing particular dopants/defects and structure regulation. Herein, the recent advances regarding the rational design of carbon-based electrocatalysts for the oxygen reduction reaction and oxygen evolution reaction are summarized, with a special focus on the bifunctional applications in Zn–air and Li–air batteries. Specifically, the atomic modulation strategies to regulate the electrocatalytic activities of carbons and structure modification are summarized to gain deep insights into bifunctional mechanisms and boost advanced Zn–air and Li–air batteries. The current challenges and future perspectives are also addressed to accelerate the exploration of promising bifunctional carbon catalysts for renewable energy technologies, particularly metal–air batteries.

and sustainable energy due to the intermittent distribution of energy sources in space and time.<sup>[2,3]</sup> Among the prevailing energy conversion and storage devices, metal–air batteries with a metal anode, such as lithium, zinc, iron, aluminum, sodium, potassium, and magnesium,<sup>[4]</sup> have gained increasing interest due to the large theoretical energy density based on unlimited oxygen supply from atmosphere as well as empowered by the open structure of the air electrode.<sup>[5,6]</sup> Especially, the lithium–air (Li–air) battery has the largest theoretical energy density ( $\approx 5928 \text{ Wh kg}^{-1}$ ) and a large cell voltage ( $\approx 2.96 \text{ V}$ ), while zinc is a cost-effective alternative with a comparable energy density ( $\approx 1218 \text{ Wh kg}^{-1}$ ) and large volumetric energy density ( $\approx 6136 \text{ Wh L}^{-1}$ ) to those of Li–air batteries.<sup>[7]</sup> Both Zn–air and Li–air batteries have received extensive attention recently with the rapid development of advanced electrocatalysts for air

## 1. Introduction

The sustainable development of modern society requires sustainable supply of clean energy sources from sunlight, wind, hydroelectricity, geothermal, heat, and biofuels. It is urgent to replace traditional fossil fuels due to their detrimental effects on the environment.<sup>[1,2]</sup> Therefore, massive efforts have been devoted to developing advanced techniques for harvesting clean

electrodes, emerging electrolytes, and nanostructured metal anodes.<sup>[7–9]</sup> However, the sluggish reaction kinetics of oxygen reactions involving oxygen reduction reaction (ORR) and oxygen evolution reaction (OER) in air electrodes require the exploitation of efficient bifunctional electrocatalysts with good stability for enhancing the battery performance.<sup>[10–12]</sup>

Both noble metals and metal oxides (e.g., Pt, IrO<sub>2</sub>, and RuO<sub>2</sub>) were commonly used as efficient electrocatalysts

Dr. Y. Huang, Prof. Y. Wang  
CAS Key Laboratory of Design and Assembly of Functional Nanostructures, and Fujian Provincial Key Laboratory of Nanomaterials State Key Laboratory of Structural Chemistry  
Fujian Institute of Research on the Structure of Matter  
Chinese Academy of Sciences  
Fuzhou, Fujian 350002, China  
E-mail: wangyb@fjirsm.ac.cn

Y. Wang, Dr. J. Wang, Prof. J. Zhang  
Key Laboratory for Colloid and Interface Chemistry (Ministry of Education) School of Chemistry and Chemical Engineering and Key Laboratory for Liquid-Solid Structural Evolution and Processing of Materials (Ministry of Education)  
Shandong University  
Jinan 250100, China  
E-mail: jtzhang@sdu.edu.cn

Dr. C. Tang, Prof. Q. Zhang  
Beijing Key Laboratory of Green Chemical Reaction Engineering and Technology  
Department of Chemical Engineering  
Tsinghua University  
Beijing 100084, China  
E-mail: zhang-qiang@mails.tsinghua.edu.cn

 The ORCID identification number(s) for the author(s) of this article can be found under <https://doi.org/10.1002/adma.201803800>.

DOI: 10.1002/adma.201803800

for ORR and OER, respectively.<sup>[13,14]</sup> Considering the scarcity<sup>[6]</sup> and monofunctionality,<sup>[15]</sup> it is imperative to enhance the catalytic efficiency and utilization of noble-metal-based catalysts via the rational design of structure and composition.<sup>[14,16]</sup> Alternatively, the exploitation of efficient and stable non-noble-metal-based electrocatalysts is also highly desirable for the rapid progress of advanced energy devices, such as metal–air batteries. Metal-free carbon electrocatalyst was first considered to catalyze ORR by Dai and co-workers in 2009. The aligned CNT electrocatalyst exhibited good ORR activity and a long-term stability in comparison with the commercial Pt/C catalyst (20 wt% Pt/C).<sup>[17]</sup> Following the pioneer work, carbon-based bifunctional catalysts for both ORR and OER were considered owing to their unique features:<sup>[10,18–21]</sup> (i) Structural diversity of carbon materials, from 0D (e.g., fullerene), 1D (e.g., carbon nanotubes (CNT)), 2D (e.g., graphene) to 3D porous carbon nanostructures, enables their better adaptability in the applications of air electrodes; (ii) good conductivity benefits to the rapid electron transfer for enhancing electrocatalytic activity; (iii) low cost due to the abundant carbon resources enables high economic viability for practical applications in metal–air batteries.

More importantly, tailoring surface chemistry and structure of carbon catalysts can be easily implemented by heteroatom doping or creating surface and edge defects.<sup>[22–24]</sup> The essence of both heteroatom doping and surface/edge defects is to charge the charge/spin status via atomic modulation strategies. Consequently, the electrocatalytic activities of carbon materials generally can be understood on the basis of the charge/spin redistribution mechanism induced by the presence of defects.<sup>[11,25]</sup> The local physical and chemical properties of carbon electrocatalysts regulated by heteroatoms and other defects have been carefully investigated through novel characterization techniques and/or theoretical principles. There is significant research progress on the defects design of carbon materials for enhancing electrocatalytic activities toward ORR and OER via the atomic modulation and structural design. Especially, the atomic configurations are strongly dependent on the synthesis processes. The electronic conductivity, reactivity, and corrosion-resistance are highly depended on the structure of carbon-based electrocatalysts.<sup>[11,20,26,27]</sup> With the rapid increasing research volume devoted to the carbon materials for electrocatalysis, a timely progress on this flourishing field, with regard to intrinsic relation of synthesis–structure–properties and the design principles for metal–air battery applications, is highly desirable.

The goal of this research progress is to gain a clear route for the design of metal-free carbon-based materials from synthesis and mechanism understanding to the promising applications for metal–air batteries. With the fundamental introduction on the electrocatalytic mechanism of carbon materials, we summarize the recent significant advances mainly on the carbon electrocatalysts for advanced Zn–air and Li–air batteries, with a special emphasis on the design of bifunctional carbon catalysts via the atomic modulation and structural design. The challenges and perspectives are also included to boost the exploitation of novel carbon electrocatalysts for promising applications.



**Qiang Zhang** started his study at Tsinghua University, China, in 2000. After receiving his Ph.D. in 2009, he worked at Case Western Reserve University, USA, and the Fritz Haber Institute of the Max Planck Society, Germany. He was appointed as a faculty member at Tsinghua University in 2011. His current research interests are energy materials, including lithium–sulfur batteries, lithium metal, ORR/OER electrocatalysis, and 3D graphene-based nanostructures.



**Yaobing Wang** is a professor at Fujian Institute of Research on the Structure of Matter, Chinese Academy of Sciences. He received his Ph.D. from the Institute of Chemistry, Chinese Academy of Sciences. His current research is focused on synthesis of novel 2D materials and application in energy conversion and storage, especially for nitrogen reduction and carbon dioxide reduction reactions.



**Jintao Zhang** is a full professor at the School of Chemistry and Chemical Engineering, Shandong University. He obtained his Ph.D. from the National University of Singapore in 2012. Prior to joining Shandong University, he was a postdoctoral fellow at Nanyang Technological University and Case Western Reserve University, USA. His research interests include the rational design and synthesis of advanced materials for electrocatalysis, electrochemical energy storage, and conversion (e.g., metal–air batteries, supercapacitors, and fuel cells).

## 2. Atomic Modulation and Structure Design of Bifunctional Carbon Electrocatalysts

### 2.1. Mechanism Understanding on Atomic Modulation

Oxygen reduction/evolution reactions are multiphase interface electrocatalysis processes comprising several indispensable steps of mass diffusion, reactant/intermediate adsorption,

charge transfer, bond cleavage, and product desorption.<sup>[28,29]</sup> Many of these steps were dominated by electronic structure of nanocarbons. The modification of electronic structure is therefore deemed as the critical factor to regulate the intrinsic electrocatalytic activity.<sup>[30]</sup> In the pioneer work of Dai and co-workers,<sup>[31]</sup> it has been revealed that the nitrogen doping in carbon nanotubes regulated the oxygen chemisorption mode from end-on to side-on, which can effectively weaken and broken the O–O bonding and significantly boost the ORR activity. The formation of carbon atoms with positive spin/charge densities ( $\delta^+$ ) due to the presence of adjacent electron-withdrawing pyridinic N leads to the energetically favorable adsorption of O<sub>2</sub> and intermediate, OOH\*. Such carbon atoms are widely recognized as active sites for ORR.<sup>[10,32,33]</sup> However, it has been reported that the carbon atoms ( $\delta^-$ ) near the electron-donating quaternary N atoms also provide the favorable adsorption sites for anchoring O\* and OOH\* intermediates of ORR.<sup>[25c]</sup> Thus, ORR is also dependent on the quaternary N atoms.<sup>[25c,34,35]</sup> Despite this controversy, nitrogen doping is regarded as the most effective strategy to create ORR active sites in nanocarbons due to the higher electronegativity, comparable atomic size, diverse configurations, and versatile synthesis.<sup>[36]</sup> Analogous to N, heteroatoms of O, Cl, P, and B can also regulate the surface charges of sp<sup>2</sup> carbon lattice due to the difference in electronegativity, thus modifying the adsorption energy of O<sub>2</sub> and intermediates toward efficient ORR activity (Figure 1a).<sup>[10,22,37]</sup> Those positively charged

atoms ( $\delta^+$ ), either the dopants or neighboring carbon atoms, are potentially active sites. Notably, another approach named as “molecular doping” holds similar mechanism.<sup>[38]</sup> The hybridization of molecular doping components on all-carbon substrates, such as poly(diallyldimethylammonium chloride),<sup>[39]</sup> nitrobenzene,<sup>[38]</sup> and even graphene quantum dots,<sup>[22]</sup> will withdraw electrons from the conjugated nanocarbon plane and thus generate carbon atoms with positive surface charge ( $\delta^+$ ), leading to favorable adsorption sites and boosted ORR activity. In the case of S-doping, the negligible electronegativity difference between S and C atoms is not able to change the surface charge status. However, the electron spin effects in the favorable O<sub>2</sub> adsorption on S-doped carbon are identified as the electrocatalytic activity origin for ORR instead of the charge redistribution.<sup>[40–42]</sup> In addition to the optimized surface adsorption properties, dopants can also polarize the molecular orbitals to shorten the bandgap.<sup>[21,40,43]</sup> Therefore, the enhanced electron transfer from nanocarbon to the adsorbed O<sub>2</sub> would be beneficial to form OOH\* for expediting ORR.

Generally, the oxygen evolution reaction rate is determined by transforming O\* to OOH\*. Carbon atoms with positive charges ( $\delta^+$ ) induced by electron-withdrawing species, such as pyridinic N,<sup>[25c,44]</sup> C=O,<sup>[45,46]</sup> C–S–C,<sup>[35,47]</sup> and surface polar oxygen groups,<sup>[48]</sup> are revealed as active sites for OER in alkaline media, because of the favorable adsorption of hydroxyl species (e.g., OH<sup>-</sup>) on the carbon atoms with positive charges ( $\delta^+$ ). Additionally, heteroatoms would accelerate the electron transfer

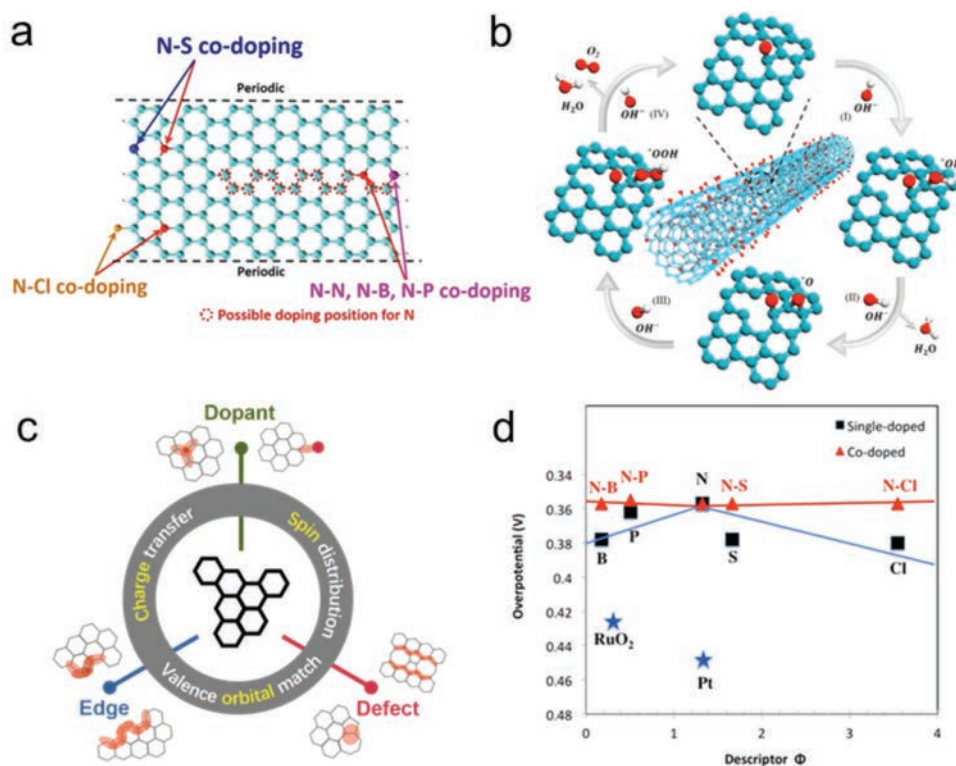


**Figure 1.** a) Schematic illustration of the N,X-codoped graphene nanoribbons with the possible dopant positions (X = B, P, S, and Cl). Reproduced with permission.<sup>[37]</sup> Copyright 2016, American Chemical Society. b) A proposed OER pathway on the C=O groups on carbon nanotubes. Reproduced with permission.<sup>[46]</sup> Copyright 2017, American Chemical Society. c) Different active sites and underlying mechanism for metal-free carbon catalysts. Reproduced with permission.<sup>[57]</sup> Copyright 2017, Wiley-VCH. d) The lower limit of ORR/OER overpotentials for single- and dual-doped graphene structures. Reproduced with permission.<sup>[37]</sup> Copyright 2016, American Chemical Society.

from the adsorbed OH\* to a catalyst, thus effectively triggering the generation of O\* and OOH\* intermediates.<sup>[25c]</sup> Notably, heteroatom location has significant influence on the charge dispersion. For instance, electron-withdrawing ketone groups, as determined by ex situ X-ray photoelectron spectroscopy and in situ electrochemical impedance spectroscopy, can reduce the electron density at the *meta*-position carbon atoms for the adsorption of OH\* species and also accelerate the reaction with another OH<sup>-</sup> to form O\* species, whereas the *ortho*-position and *para*-position carbon atoms are less affected (Figure 1b).<sup>[45]</sup> Both OH\* and OOH\* would be stabilized by hydrogen bonding, which regulates the adsorption energies of intermediates and eventually improves the OER activity, as demonstrated by noncovalently wrapped oxygen-containing polymers.<sup>[49]</sup> In addition to activity promotion mechanism, stability enhancement should also be noted, since OER usually takes place at high potentials above 1.3 V versus reversible hydrogen electrode (RHE), and carbon materials would be susceptible to significant corrosion at the potentials.<sup>[44,49]</sup> Engineering of nanocarbon toward robust structural features and active sites is thus a prerequisite. In this regard, high graphitization of the nanocarbon electrocatalysts obtained by high-temperature treatment with more stable doping configuration is beneficial to the improved durability.<sup>[18,27]</sup> Besides, regulation over unstable active sites still holds promise. For instance, nitrogen doping with a high content (5.9 at%) induces overall greater charge redistribution and lead to increased C1s binding energy with inhibited carbon corrosion.<sup>[25c]</sup> More stable C–S–C sites obtained by a sequential bidoping strategy can impressively retain 100% of OER stability after 75 h.<sup>[47]</sup>

In addition to the various types, contents, and configurations, the characteristics of doping locations, multidoping, and topological defects also contribute to the different catalytic activities toward both ORR and OER. First, theoretical investigations revealed that the overpotentials increased with enlarging the distance between the doped atoms and the graphene edge.<sup>[37]</sup> The dopants located in the distance range of <3 Å from the edge of sp<sup>2</sup> carbon lattice are identified to be the most active sites with faster electron transfer rate and optimized adsorption of intermediates.<sup>[10,18,37,50]</sup> In addition to the widely accepted factor of electronegativity, the electron affinity of dopants is also suggested to adopt as a comprehensive activity descriptor for predicating the ORR/OER bifunctional activities of metal-free carbons. Second, compared to monodoping, multidoping with several heteroatoms is revealed to be more promising for highly effective nanocarbon-based catalysts, such as B/N,<sup>[51,52]</sup> S/N,<sup>[42]</sup> N/P,<sup>[53]</sup> and N/P/O-codoped carbon for ORR, and N/O,<sup>[54]</sup> N/P,<sup>[55]</sup> and N/S-codoped nanocarbon<sup>[56]</sup> for OER. The synergistic effects between codopants induce larger charge redistribution and more active sites, and the distance between codopants is also critical to such synergistic effects and resultant activity.<sup>[37,52]</sup> Finally, dopant-free topological defects in nanostructured carbons are recently revealed to be possible active sites for ORR/OER both theoretically and experimentally,<sup>[57]</sup> such as pentagon and zigzag edge defects,<sup>[58,59]</sup> edge-adjacent pentagon and heptagon structures,<sup>[57]</sup> and pentagon–octagon–pentagon conjunction.<sup>[60]</sup> The zigzag edges with unpaired  $\pi$  electrons substantially decrease the reaction free energy and facilitate the electron transfer for forming OOH\*.<sup>[58]</sup> The

adjacent carbon rings were supposed to generate spatial curvatures and a permanent dipole moment due to different electron densities, thereby leading to a moderate adsorption and higher activity.<sup>[57]</sup> Remarkably, there are also edge effect (with favorable edge structures)<sup>[59]</sup> and synergistic effect (with dopants)<sup>[61]</sup> in topological defect-induced activity. Overall, all these proposed active origins (dopants, edges, defects, etc.) have been well demonstrated to enhance the electrocatalytic activity to ORR and/or OER under the similar mechanism, by modifying the charge/spin distribution of carbon atoms and thus optimizing the chemisorption of intermediates (Figure 1c).<sup>[57]</sup>

Although the activity mechanism for ORR/OER is almost the same as discussed above, it is notable that most efficient sites for ORR and OER are separated from each other in bifunctional nanocarbons.<sup>[50]</sup> For instance, the X-ray absorption near-edge structure spectroscopic measurements demonstrated that ORR occurred at the n-type domains near electron-donating quaternary N sites, while OER proceeded at the p-type domains near electron-withdrawing pyridinic N and C=O moieties in N-doped graphene.<sup>[25c]</sup> In N/P-codoped graphene, the most active sites for ORR are located at edges near N doping, while those edge sites near the N/P-coupled structure are efficient to OER.<sup>[18]</sup> Therefore, ORR/OER dual sites are expected to be rationally combined together for efficient bifunctional catalysts, such as the coexistence of multiple active sites (different dopants, edges, topological defects, surface functional groups, etc.). One of the most versatile, controllable, and effective strategy is multidoping with codopants of relatively different chemical properties, fully utilized synergistic and edge effects (Figure 1d).<sup>[37]</sup> So far, a series of metal-free multidoped nanocarbon catalysts have been reported with remarkable ORR/OER bifunctional electrocatalytic activities, such as N/P-doped mesoporous carbon,<sup>[18]</sup> N/P-doped graphene/carbon nanosheets,<sup>[62]</sup> N/P/F-doped graphene,<sup>[63]</sup> N/S-doped carbon nanosheets,<sup>[64]</sup> P-doped g-C<sub>3</sub>N<sub>4</sub>,<sup>[65]</sup> N/S-doped porous carbon,<sup>[35]</sup> and N/P comodified carbon nanodots.<sup>[33]</sup>

Besides the favorably modified electronic structures for accelerated surface reactions, rationally engineered hierarchical morphology, and electrode interface are also critical to the mass diffusion, electron transfer, and adsorption/desorption,<sup>[11,29]</sup> which ultimately affect the electrocatalytic activity. Several important structural features should be taken into consideration, including high graphitization for good electrical conductivity,<sup>[18,47]</sup> well-developed porosity for smooth electrolyte diffusion,<sup>[35,42,54,66]</sup> high surface area with fully exposed active sites,<sup>[67]</sup> functionalized surface for improved hydrophilicity and oxygenophilicity,<sup>[18,48,54,68]</sup> freestanding electrode for increased active sites, enhanced stability and practical utilization,<sup>[69,70]</sup> and so on.

## 2.2. Structure Design Strategies

On the basis of the fundamental mechanism discussed above, particular structure design strategies for highly active ORR/OER bifunctional electrocatalysts are desired to achieve the high-content doping, multidoping/defects with synergy, high graphitization, and hierarchical porosity in carbon-based electrocatalysts. Furthermore, general merits of macrostructures

for increasing the utilization efficiency of intrinsic active sites should be combined with the atomic modulation and microstructure design.

To achieve high-content heteroatom doping, gaseous nitrogen sources, such as ammonia<sup>[69,71–76]</sup> and cyano fragments derived from cyanamide and C<sub>3</sub>N<sub>4</sub> at an elevated temperature,<sup>[64,77–79]</sup> were employed for doping of nitrogen into carbon under pyrolysis conditions. This versatile strategy for nitrogen doping, usually accompanies with generation of various defects and porous structure in micro-/macroscale across the carbon scaffolds via carbon etching reaction.<sup>[71]</sup> However, the utilization of nitrogen source in this route is actually rather low, along with some pollution emission. Meanwhile, the category of doped nitrogen is nearly uncontrollable. These drawbacks can be eliminated to some extent by employing core–shell type carbon/nitrogen complex as precursors for pyrolysis, for example, glucose-coated g-C<sub>3</sub>N<sub>4</sub><sup>[80]</sup> and polydopamine-covered graphene.<sup>[81]</sup> Organic compounds involving dopamine, glucosamine,<sup>[82]</sup> and aniline<sup>[83]</sup> can adsorb and polymerize on various substrates/templates such as graphene, Te nanowires, and SiO<sub>2</sub> aggregation, to ultimately form the ideal carbon nanoarchitectures with good structural unity and high porosity.

The interplay between multidoping and various active sites is more important than the apparent content. Efficient approaches for bi-/multidoping, such as combination of single-doping processes, and use of sole precursor containing multiple heteroatoms, like thiocyanic acid,<sup>[84]</sup> biomass horn,<sup>[85]</sup> cystine,<sup>[86]</sup> and N-methyl pyrrolidone,<sup>[87]</sup> were widely reported, with less distinctions on structure regulation. For example, those nitrogen-containing polymers can be further grafted with other heteroatom organics (e.g., thiol),<sup>[88]</sup> providing a general bi-/multiatom doping approach to adjusting the different heteroatom categories. We have described a self-template route to synthesize polyaniline (PANI) aerogels, in which a soft-template, phytic acid was used to fabricate porous PANI foam.<sup>[18]</sup> Subsequently, the pyrolysis of the PANI aerogel leads to the easy formation of N,P-codoped mesoporous nanocarbon (NPMC) foams (Figure 2a). It is notable that pyrolysis at an elevated temperature generally leads to loss of heteroatoms from the carbon framework, which instead, generate topological defects and enhance the electronic conductivity due to the improved graphitization.<sup>[18,91]</sup> We also demonstrated that defects and nitrogen doping were both formed in the graphene mesh (NGM) after direct carbonization of rice, melamine, and Mg(OH)<sub>2</sub> as template (Figure 2b).<sup>[89]</sup> The combined contribution between nitrogen doping and edge defects was revealed for oxygen electrocatalysis in NGM. Furthermore, doping and defects usually supplement each other. For instance, the low-temperature ball-milling can generate abundant edges, serving further as vulnerable regions for doping of heteroatoms such as P<sup>[92]</sup> and N at high content level of 11.4%.<sup>[93]</sup> This is a promising route because the heteroatom doping adjacent to edges/defects often express potential catalytic activity for ORR/OER as aforementioned. Other methods such as plasma etching,<sup>[94]</sup> superdoping approach based on fluorinated graphene,<sup>[23]</sup> and heteroatom leaching/substitution approach from carbide<sup>[95]</sup> were also developed to create defects and/or high-content heteroatom doping.

The mass and electron transfer in carbon materials can be accelerated through the fabrication of 3D porous structure and the optimization of graphitization degree, respectively. To create pores, templating and chemical etching approaches are most commonly employed. For instance, monodispersed SiO<sub>2</sub> nanosphere<sup>[96]</sup> and polystyrene (PS) spheres<sup>[97]</sup> were recently reported as templates, which can be readily removed by HF/NaOH and N,N-dimethylformamide (DMF), respectively, to construct homogeneous porosity across the carbon frameworks. Recently, Hu et al.<sup>[88]</sup> reported that melamine was used as the carbon/nitrogen source by templating KCl-Ni<sub>2</sub>SO<sub>4</sub> to obtain N,S-codoped graphitic sheets (SHG) with stereoscopic holes via direct pyrolysis and purification processes (see Figure 2c). SHG with a large surface area of 576 m<sup>2</sup> g<sup>-1</sup>, a wide pore size distribution from 3 to 30 nm, and a large pore volume of 1.40 cm<sup>3</sup> g<sup>-1</sup> has been synthesized for facilitating ORR/OER electrocatalysis. Compared to the homogeneous porosity by template approach, hierarchically porous structures can be fabricated through chemical etching route, in which chemicals such as KOH,<sup>[72]</sup> CO<sub>2</sub>,<sup>[73]</sup> and NH<sub>3</sub><sup>[79]</sup> were commonly used as etching agents at elevated temperatures. Notably, pyrolysis of organic precursors could spontaneously generate abundant pores in the graphitic planes, mainly due to the removal of volatile species like CO and CO<sub>2</sub>. For instance, the NPMC foams derived from PANI/phytic acid aerogel carbonization exhibited an ultrahigh surface area of 1548 m<sup>2</sup> g<sup>-1</sup>, and a large pore volume and a small pore size less than 10 nm, benefiting for electrocatalytic applications.<sup>[18]</sup> Optimization of pore structure can not only facilitate mass diffusion, but also enlarge the specific surface area to expose more intrinsic active sites.

To accelerate the electron transfer, highly graphitic carbons such as CNTs and graphene are highly recommended.<sup>[76,77,85]</sup> These nanocarbons render excellent stability against oxidative corrosion during ORR/OER at high potentials, and can serve as alternative substrates because of the high surface area, uniform 1D/2D structure, modifiable surfaces with various functional groups, and flexibility for assembly of 3D porous frameworks. As a typical example, N-doped graphene/single-walled carbon nanotube hybrid (NGSH) has been fabricated through chemical vapor deposition (CVD) on layered double hydroxides (LDHs) derived catalysts (Figure 2d).<sup>[76]</sup> The porous NGSHs exhibit a large surface area and a high graphitic degree, thus rendering excellent ORR/OER bifunctional activity. Although innumerable novel carbon materials have been derived from metal–organic frameworks,<sup>[11]</sup> polymers,<sup>[79,98]</sup> and cost-effective biomass such as sucrose,<sup>[84]</sup> cotton,<sup>[71]</sup> cellulose,<sup>[72,74]</sup> glucose,<sup>[73]</sup> and artemia cyst shells,<sup>[99]</sup> it is highly desirable to combine the merits of porosity and high graphitization, 3D assembly of these promising carbons for electrocatalytic applications.

The metal–air battery is a big family of electrochemical energy devices on the basis of the redox reactions between a specific metal (e.g., Zn, Li, Na, K, Fe, Al) and oxygen in an electrolyte. Although different metals and electrolytes would be used in metal–air batteries, the battery performances including the energy density and cycling stability are highly dependent on the composition and structure of air electrodes for oxygen

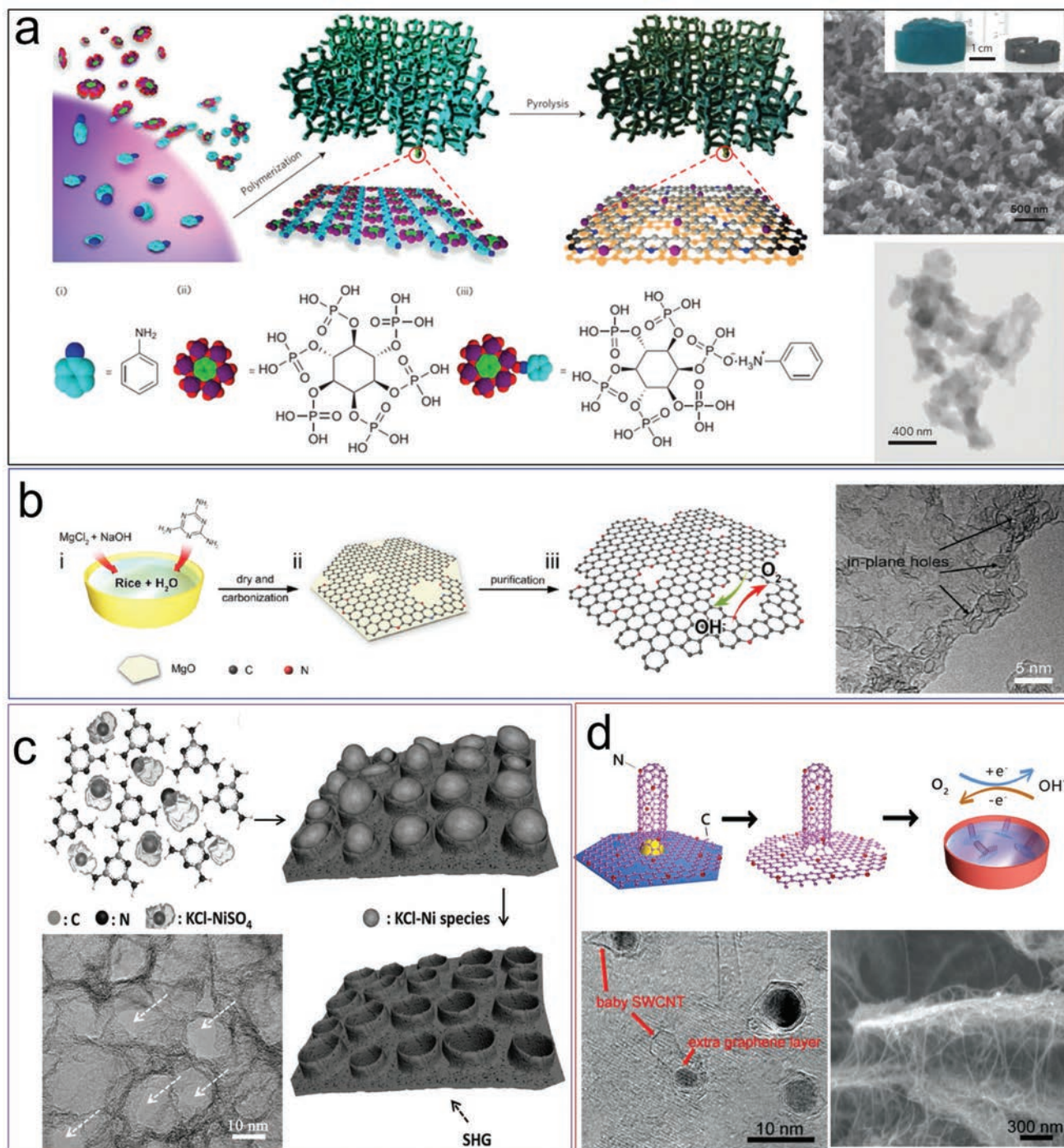


**Figure 2.** Schematic representation for fabrication procedures and corresponding structure characterization of various carbon materials. a) N,P-codoped mesoporous nanocarbon (NPMC) foams. Reproduced with permission.<sup>[13]</sup> Copyright 2015, Nature Publishing Group. b) Heteroatom-doped and edge-rich graphene (NGM). Reproduced with permission.<sup>[89]</sup> Copyright 2016, Wiley-VCH. c) N,S-codoped graphitic sheets (SHG). Adapted with permission.<sup>[90]</sup> Copyright 2017, Wiley-VCH. d) Nitrogen-doped graphene/carbon nanotube hybrids. Adapted with permission.<sup>[76]</sup> Copyright 2014, Wiley-VCH.

electrocatalysis. Carbon materials with good electrocatalytic activities have been used as air electrode electrocatalysts to fabricate various metal–air batteries. For example, the carbon composite electrode was used to fabricate a thin-film Li–air battery by using a solid polymer electrolyte in 1996.<sup>[100]</sup> Recently,

carbons with/without nitrogen doping were recently assembled as air electrodes for a Na–air battery.<sup>[101–104]</sup> However, carbon electrocatalysts are intensively used in Zn–air and Li–air batteries. Thus, the following sections are mainly focused on these two types of metal–air batteries.

### 3. Carbon Electrocatalysts for Zn–Air Batteries (ZABs)

#### 3.1. Basic Configuration of a Zn–Air Battery

A typical ZAB comprises of four components: Zn electrode, electrolyte, separator, and air electrode (**Figure 3a**). During the discharge process, the atmosphere oxygen permeates through gas diffusion layer (GDL) to electrocatalyst surface and is reduced to hydroxyl ions ( $\text{OH}^-$ ) at the air electrode. Meanwhile, the metallic zinc is oxidized to  $\text{Zn}^{2+}$  with the release of electron via the external circuit. The dissolved  $\text{Zn}^{2+}$  ions further coordinate with  $\text{OH}^-$  to form solvable  $\text{Zn}(\text{OH})_4^{2-}$ . During the charge process, reversible reactions occur with zinc plating on the anode and oxygen evolution on the electrocatalyst surface of an air electrode.<sup>[107,108]</sup> Each aforesaid component could independently influence the overall performance of the battery.

In addition to the planar zinc, other nano-/microstructured zinc electrodes with higher surface areas, in the form of nanoparticles, fibers, rods, and flakes, have been investigated to improve the metal utilization for the enhancement of specific capacity.<sup>[108,109]</sup> In spite of the good reversibility of zinc redox reactions, the concentration gradient of  $\text{Zn}(\text{OH})_4^{2-}$  ions on zinc electrode surface, and the uneven current density for dissolution/deposition give rise to zinc dendrite growth, shape change, and side reactions (e.g., hydrogen evolution reaction (HER)).<sup>[110]</sup> Therefore, effective approaches are requisite to address such issues on the basis of the basic principles: (i) the incorporation of additives, such as polymer binders and carbons in zinc electrode to enhance the mechanical strength

and conductivity, and improve the utilization; (ii) the alloying of zinc electrode with semiconductor metal (e.g., Bi, Sn, In) with high HER overpotentials in order to suppress hydrogen evolution; (iii) the coating of zinc electrode with additives such as polyaniline and polypyrrole to block discharge product migration, thus suppressing the dendrite growth; (iv) the optimization of electrolyte for improving the performance of both Zn and air electrodes.<sup>[108]</sup> Generally, the cost-efficient KOH solution (30 wt%) with good ionic conductivity of  $\text{K}^+$  relative to  $\text{Na}^+$ , and high solubility for zinc salts is used as the efficient electrolyte.<sup>[108]</sup> Besides, Zn salts (e.g.,  $\text{Zn}(\text{AC})_2$ ,  $\text{ZnCl}_2$ )<sup>[90]</sup> and corrosion inhibitors (e.g., poly(ethylene glycol) (PEG), organic acid) are generally added to improve the electrochemical reversibility and alleviate the side reactions.<sup>[7]</sup> For the membrane separator, an applicable candidate should meet the basic requirements including superior stability in alkaline electrolyte, high ionic conductivity, good electrical resistance, sufficient mechanical strength to retard dendrite perforation, and fine porosity to block the zinc ion permeation. Nonwoven porous polymer membranes including polyamide,<sup>[111]</sup> polyethylene, poly(vinyl alcohol), polypropylene,<sup>[112]</sup> and poly(acrylic acid) are commonly used in Zn–air batteries to enhance the migration of hydroxyl ions and to regulate electron/oxygen/zincate ion transfer.<sup>[7,113]</sup>

As the crucial component of Zn–air batteries, the air electrode includes three parts: hydrophobic GDL, current collectors, and active electrocatalyst layers. The GDL with abundant oxygen diffusion channels is commonly composed of porous carbon-based electrocatalysts (e.g., acetylene black, activated charcoal) and waterproof polymer (e.g., poly(tetrafluoroethylene) (PTFE))

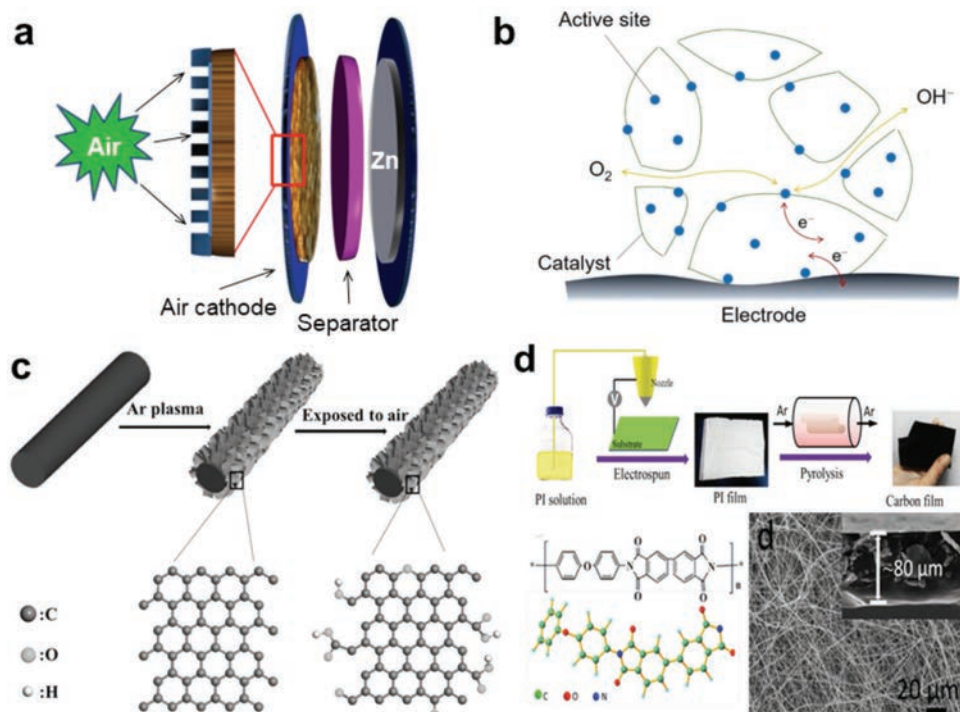


**Figure 3.** a) Schematic illustration of a Zn–air battery. Adapted with permission.<sup>[18]</sup> Copyright 2015, Nature Publishing Group. b) Schematic illustration of the electrocatalysis process in ORR and OER. Reproduced with permission.<sup>[105]</sup> Copyright 2018, Wiley-VCH. c) In situ exfoliation for preparation of the edge-rich and oxygen-functionalized graphene/carbon fiber electrode. Reproduced with permission.<sup>[106]</sup> Copyright 2017, Wiley-VCH. d) Nanoporous carbon nanofiber films (NCNFs), and their electron microscopy images. Reproduced with permission.<sup>[33]</sup> Copyright 2016, Wiley-VCH.

to regulate the gas diffusion, and suppress electrolyte leakage/evaporation during discharge/charge processes.<sup>[7]</sup> The catalyst layer is responsible for enhancing O<sub>2</sub> reduction and evolution efficiency to lower the voltage gap between charging and discharging processes, and has to endure the harsh oxidative/reductive conditions in alkaline electrolytes.<sup>[7]</sup> Till now, most of the emerging carbon materials for catalyst layers are still in the form of fine powders. Therefore, the air electrode is usually fabricated by drop-casting of electrocatalysts on a current collector with GDLs, which leads to some adverse factors such as uncontrolled material distribution, a plenty of dead volumes, losing active sites covered by binders, and material peeling due to gas evolution.<sup>[114]</sup> Given that the three-phase interface is prerequisite for ORR and OER (Figure 3b), rational design of multiphase interface with large specific surface area is crucial to optimize battery performance.<sup>[108]</sup>

Carbon-based catalysts exhibit good compatibility with the hydrophobic gas diffusion layers, which often adopt commercially available carbon cloth due to its flexibility and high shape conformability.<sup>[115]</sup> Hydrophilic carbon catalysts can directly grow on the conductive porous substrates,<sup>[116]</sup> without using any ancillary additive. This configuration can afford not only high accessibility to the multiphase active sites, but also a low interfacial contact resistance, benefiting to the large-scale fabrication of air electrodes. Other than this, the in situ growing of carbon-based materials on the bendable substrates enables the successful design of flexible air electrodes, which is indispensable in portable electronic devices.<sup>[117,118]</sup> Liu et al.<sup>[114]</sup> employed an in situ technology with Ar plasma treatment to cultivate edge-rich graphene with oxygenated groups on carbon cloth (Figure 3c), which directly served as bifunctional OER/ORR electrode. Recently, the fabrication of flexible air

electrode has also been advocated along with the development of advanced technologies such as silk-screen printing<sup>[33]</sup> and vacuum filtration.<sup>[75]</sup> We have developed an electrospun-pyrolysis route to prepare an integrated bifunctional air electrode (Figure 3d).<sup>[33]</sup> Typically, a polyimide (PI) film was prepared by the electrospun process, and the high-temperature pyrolysis was followed to prepare nanoporous nitrogen-doped carbon nanofiber films (NCNFs). The porous film with a large surface area of over 1000 m<sup>2</sup> g<sup>-1</sup> was directly employed as an air electrode to fabricate flexible Zn–air batteries. These integrated electrodes without nonconductive additive afford more accessible active sites and favorable contact resistance, thus facilitating the high performance of Zn–air batteries.

### 3.2. Primary and Mechanically Rechargeable Zn–Air Batteries

An ORR catalyst in an air electrode is the heart of a primary and mechanically rechargeable Zn–air battery.<sup>[18,119]</sup> Exploring high-efficient catalysts for reducing oxygen into water is indispensable to improve the energy conversion efficiency in a Zn–air battery.<sup>[107]</sup> Since the comparable and even better catalytic activity than that of Pt/C electrocatalyst,<sup>[112,117,120]</sup> various carbons doped with various heteroatoms have been synthesized and applied as electrocatalysts in Zn–air batteries.<sup>[121]</sup> For instance, the Zn–air battery equipped with bamboo-like NCNTs electrocatalyst in air electrode exhibited a high power density of 69.5 mW cm<sup>-2</sup> in 6.0 M KOH solution.<sup>[122]</sup> Hierarchically porous N-doped carbon by polymerization of *o*-phenylenediamine (denoted as PoPD, see Figure 4a) also exhibited comparable ORR activity with Pt/C, on account of its high surface area of 1280 m<sup>2</sup> g<sup>-1</sup> generated by combination of silica

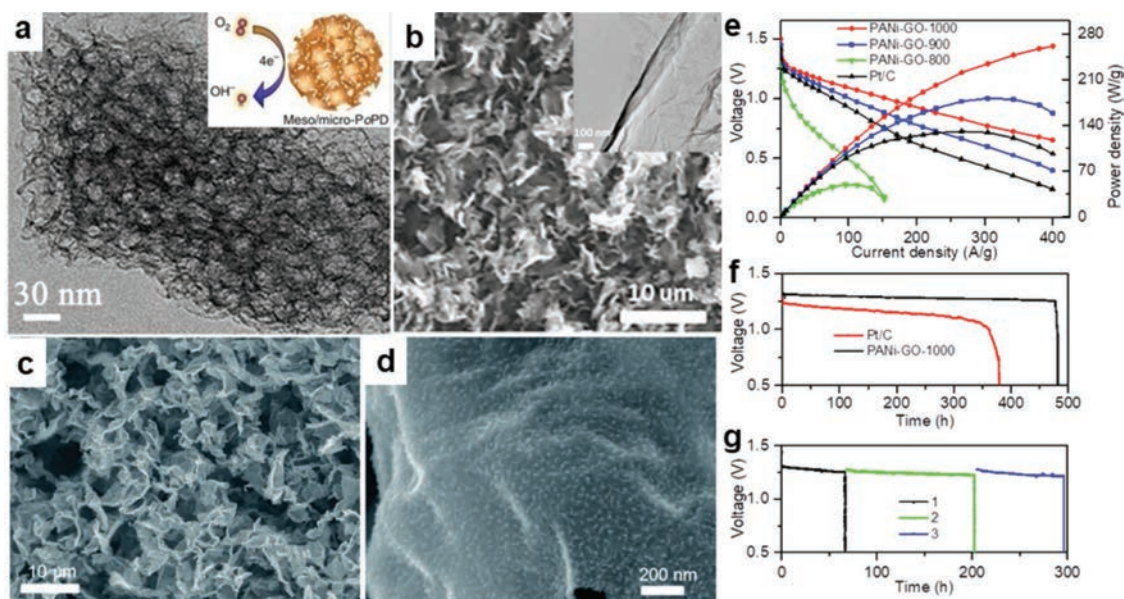


**Figure 4.** a) TEM images of meso/micro-PoPD, the inset shows the schematic diagram of meso/micro-PoPD. Adapted with permission.<sup>[123]</sup> Copyright 2014, Nature Publishing group. b) SEM images of pyrolysis MP5A/GO, inset shows TEM images of graphitic sheet. Adapted with permission.<sup>[53]</sup> Copyright 2016, Wiley-VCH. c,d) SEM images of PANI-GO-1000 Galvanostatic discharge curves of PoPD-based ZAB at 100 mA cm<sup>-2</sup>. e) Polarization and power density curves and f) the discharging curves of Zn–air batteries assembled with the as-prepared electrocatalysts and Pt/C. g) Long-time durability of the Zn–air battery by mechanically replacing Zn and electrolyte. c–g) Reproduced with permission.<sup>[124]</sup> Copyright 2018, Science China Press Co., Ltd.

hard template processing and  $\text{NH}_3$  etching.<sup>[123]</sup> Notably, the Zn–air battery exhibited superior discharge performance with a large gravimetric energy density of  $800 \text{ Wh kg}^{-1}$  at current densities of  $10 \text{ mA cm}^{-2}$ , respectively, comparable to those of Pt/C, which was contributed to the hierarchically porous structure. Furthermore, the air electrode worked robustly for 100 h without any voltage loss by mechanically replenishing the zinc anode and electrolyte. Recently, by controllable self-assembly and pyrolysis of melamine/phytic acid supermolecular aggregate on graphene oxide sheets (MPSA/GO), we synthesized 3D N,P-codoped carbon networks composed of thin graphitic sheets with wrinkles (Figure 4b). The MPSA/GO exhibited a favorable ORR activity in terms of more positive onset and half-wave potentials than those of Pt/C electrocatalyst. Owing to the robust activity to ORR and porous architecture, Zn–air batteries with an MPSA/GO electrocatalyst in the air electrode exhibited a high peak power density of  $310 \text{ W g}^{-1}$  and an excellent discharge durability for 90 h without voltage drop, outperforming the Zn–air battery based on Pt/C ( $171 \text{ W g}^{-1}$ ).<sup>[53]</sup> More recently, PANI was coated on graphene oxide to prepare a composite aerogel via oxidative polymerization of aniline monomers in the presence of phytic acid. The carbonization of PANI and phytic acid used as nitrogen and phosphorous resources resulted in the formation of 3D N,P-codoped graphene aerogel (NPGA) at an elevated temperature (Figure 4c,d).<sup>[124]</sup> Using the NPGA electrocatalysts oxygen was reduced into water directly, suggesting the good catalytic activity to ORR. NPGA electrocatalyst in an air electrode was used to fabricate Zn–air batteries. A power density as high as  $\approx 260 \text{ W g}^{-1}$  and a good long-term stability without obvious potential decay in 450 h have been achieved, thanks to the highly porous structure and the N,P codoping (Figure 4e–g). Various nitrogen-doped carbon materials with robust ORR activity including nitrogen-doped graphene,<sup>[125]</sup> carbon fibers,<sup>[126]</sup> carbon nanofiber aerogels,<sup>[74]</sup> binary and ternary-doped carbons,<sup>[127,128]</sup> other heteroatom-doped carbon,<sup>[129]</sup> and defect carbonaceous materials<sup>[90,130]</sup> have been demonstrated as efficient catalysts in Zn–air batteries.<sup>[53,112]</sup>

### 3.3. Electrically Rechargeable Zn–Air Batteries

In comparison with primary and mechanically rechargeable Zn–air batteries, electrically rechargeable Zn–air batteries favor facile design in battery configuration and recycling without additional disassembly process. Electrically rechargeable Zn–air batteries require an efficient bifunctional air electrode for both ORR and OER, which is quite challenging because of the kinetically sluggish redox processes of such reactions and the corrosive/oxidative chemical/electrochemical environment. High-efficiency electrocatalysts for air electrode should not only execute ORR/OER with high efficiency and good reversibility, but also reduce the potential gap between charging and discharging process. To reveal the reaction mechanisms, the combination of rotating ring-disk electrode with a linear sweep voltammetry method is generally used to determine the intermediates (e.g., peroxide) and the conversion efficiency for both ORR and OER. For the detailed measurements, readers are referred to the previous references.<sup>[107,131]</sup>

For the bifunctional electrocatalysts, the potential difference value between the half-wave potential of ORR ( $E_{1/2}$ ) and the potential at a current density of  $10 \text{ mA cm}^{-2}$  for OER ( $E_{j=10}$ ),  $\Delta E$  is normally used to evaluate the catalytic efficiency to lower the potential gap between ORR and OER. For instance, the potential difference of only 0.77 V at the N,S-codoped graphitic sheets electrode (Figure 5a) is much smaller than those of other carbon-based materials.<sup>[88]</sup> The good bifunctional catalytic activity renders the good performance and stability of the Zn–air battery. Besides, N-doped hollow mesoporous carbon (HMC) spheres were also used as efficient bifunctional electrocatalysts in a Zn–air battery, exhibiting good reversibility.<sup>[132]</sup>

In addition to bifunctional activity, the corrosion issues of electrocatalyst layers and gas diffusion layers gravely limit the lifetime and performance of rechargeable Zn–air batteries. The use of metallic substrates such as titanium mesh, stainless-steel mesh, nickel mesh/foam, and copper foam would contribute to the better stability and higher electrical conductivity.<sup>[133]</sup> However, it is insufficient to versatily engineer the hierarchical porosity and hydrophilicity of gas diffusion layers, thereby leading to the limited utilization of electrocatalysts. Thus, highly graphitic carbon materials with a high oxidation/corrosion resistance are highly commendatory as the catalyst/diffusion layers. For instance, the aforementioned NGSH electrode<sup>[76]</sup> displayed a high current reservation of 92.1% after 16 000 s operation for ORR, better than that of Pt/C (77.9% reservation). This ORR performance in combination with its good OER activity (370 mV at  $10 \text{ mA cm}^{-2}$  in 0.1 M KOH) rendered the promising applications for rechargeable Zn–air batteries. The active sites for ORR and OER are commonly different.<sup>[64]</sup> Thus, the repeated oxidative and reductive potential cycling would induce unrecoverable damage to these sites, leading to activity attenuation.<sup>[112,134]</sup> Therefore, the protection of these active sites against electrochemical corrosion is another essential issue in catalyst design.

As mentioned above, the high-temperature thermal treatment is effective to enhance the stability and OER activity of these doped carbon material electrodes,<sup>[84,134]</sup> which boost the performance of rechargeable Zn–air batteries. For instance, N,B-codoped carbon (BNPC-1100) prepared at  $1100 \text{ }^\circ\text{C}$  exhibited a stable electrochemical behavior in a Zn–air battery,<sup>[134]</sup> with continuous operation for 100 h without obvious performance decay. The stable discharge voltage (1.14 V) for 100 h is better than that (1.12 V) of BNPC-1000 material electrode (annealing at  $1000 \text{ }^\circ\text{C}$ ), suggesting the enhanced tolerance toward carbon oxidation/corrosion during the charge/discharge cycles. Nanoporous carbon nanofiber films annealed at  $1000 \text{ }^\circ\text{C}$  (NCNF-1000) exhibited stable ORR/OER activity,<sup>[33]</sup> and excellent discharging and charging properties in a Zn–air battery. The charge and discharge potentials could be held at 1.93 and 1.20 V, respectively, at a current density of  $10 \text{ mA cm}^{-2}$ . Thus, the voltage gap was only 0.73 V and a high round-trip efficiency at 62% was obtained, better than those of Zn–air batteries with a Pt/C electrocatalyst. Furthermore, after long-term cycling (500 cycles), the Zn–air battery assembled with the NCNF-1000 electrocatalyst exhibited nearly ignorable charging potential, and a slightly decreased discharging potential. Moreover, the two high-performance NCNF-1000 Zn–air batteries in series could power a blue light-emitting

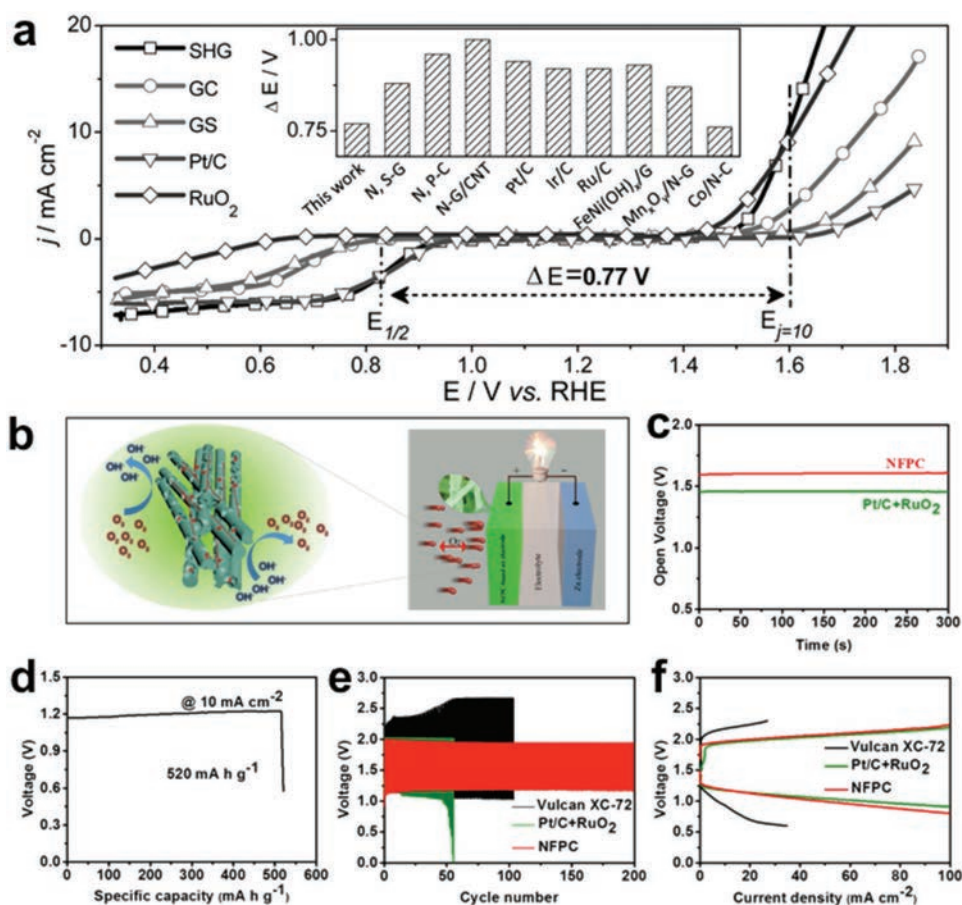


**Figure 5.** a) LSV curves for ORR and OER on different catalysts. Reproduced with permission.<sup>[90]</sup> Copyright 2016, Wiley-VCH. b) Schematic illustration of a Zn-air battery with carbon fiber catalysts, c) open-circuit potential, and d) specific capacities at a current density of 10 mA cm<sup>-2</sup> for an NFPC-based Zn-air battery; e) cycling curves of the batteries based on NFPC, Vulcan XC-72, and Pt/C+RuO<sub>2</sub> as air cathode at the current density of 10 mA cm<sup>-2</sup>, respectively; f) charge and discharge polarization curves of a Zn-air battery with NFPC, Vulcan XC-72, and Pt/C+RuO<sub>2</sub> as catalysts, respectively. b–f) Reproduced with permission.<sup>[127]</sup> Copyright 2018, Royal Society of Chemistry.

diode (LED, 3.0 V) for 12 h, demonstrating its feasibility for practical application. Water splitting can be driven by using the Zn-air battery to generate hydrogen and oxygen.<sup>[25c,89,135]</sup> Recently, an electrospinning method was used to prepare ternary-doped carbon fibers (TD-CFs). The thermal treatment resulted in the formation of efficient ORR electrocatalysts.<sup>[128]</sup> TD-CFs as air-cathode catalysts were assembled with a Zn foil to fabricate primary and rechargeable Zn-air batteries (Figure 5b–f). A specific capacity of 520 mAh g<sup>-1</sup> was achieved at a current density of 10 mA cm<sup>-2</sup>. The battery also exhibited better cycling stability in comparison with the battery using commercial electrocatalysts. For instance, phosphorus-doped g-C<sub>3</sub>N<sub>4</sub> was directly grown on CF paper to fabricate the air electrode, which showed a low interfacial contact resistance. The battery did not exhibit obvious potential decay over 50 repeated charge/discharge cycles.<sup>[115b]</sup>

Three-electrode configuration was developed recently in order to avoid direct contact between oxidative and reductive environments during charge/discharge cycling, thus enhancing the stability of air electrode for feasible applications.<sup>[8]</sup> In the three-electrode system with two air electrodes (Figure 6a), ORR and OER are separated to weaken the

negative effect of the oxidation (or reduction) process. Besides, design, optimization, and manipulation over monofunctional electrocatalyst for each air electrode are easy to perform, thereby endowing apparent improvement in battery performance including stability, energy efficiency, and cycle life. In this context, we reported that the NPMC foam prepared by pyrolysis of porous PANI was assembled in a rechargeable Zn-air battery with a tri-electrode configuration (Figure 6a).<sup>[18]</sup> After independent regulation over the mass loading of catalyst on the ORR and OER electrodes to reversibly balance ORR and OER, the battery did not display obvious potential decay over 600 discharge/charge cycles (Figure 6b), suggesting the better stability of such a Zn-air battery. Using carbon nitride sponge codoped with phosphorus and sulfur as the electrocatalyst, the battery with tri-electrode configuration<sup>[136]</sup> (Figure 6c) displayed excellent charge/discharge stability without obvious voltage decay for 500 cycles at 25 mA cm<sup>-2</sup> (Figure 6d). The two-electrode Zn-air battery assembled with the same electrocatalyst exhibited slight deterioration in charge potential for 200 discharge/charge cycles (more than 40 h). The three-electrode system is effective for improving the overall performance.<sup>[137]</sup>

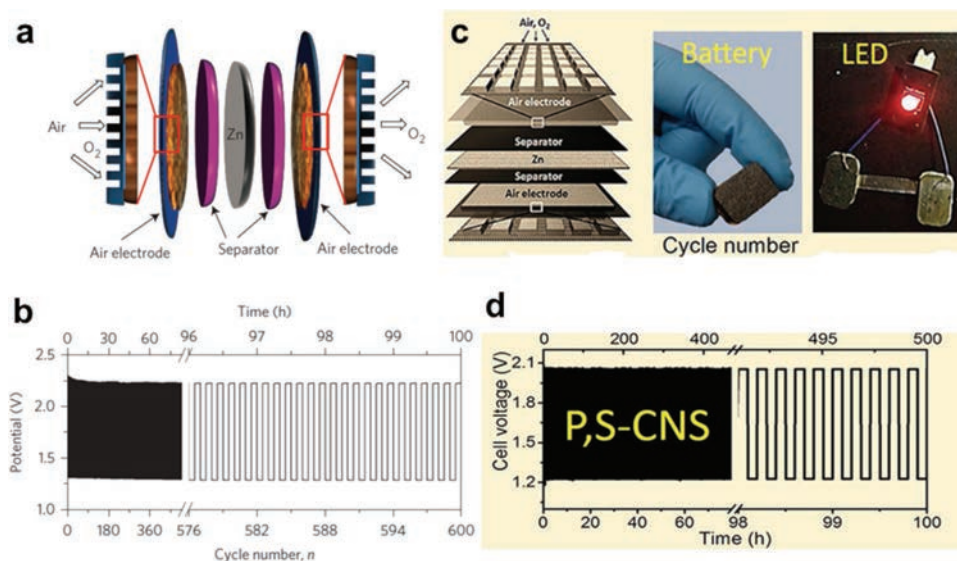


**Figure 6.** a) Schematic diagram of the basic configuration of a three-electrode Zn–air battery. b) Charge/discharge cycling curves of the above three-electrode Zn–air battery using 3D N,P-codoped mesoporous nanocarbon (NPMC-1000) for the air electrodes at a current density of  $2 \text{ mA cm}^{-2}$ . a) Adapted with permission.<sup>[18]</sup> Copyright 2015, Nature Publishing Group. b) Reproduced with permission.<sup>[18]</sup> Copyright 2015, Nature Publishing Group. c) Three-electrode configuration, 3D P,S-codoped carbon nitride sponge as bifunctional oxygen catalysts for Zn–air batteries, and d) the corresponding charge/discharge cycling curves of a three-electrode Zn–air battery. c,d) Reproduced with permission.<sup>[136]</sup> Copyright 2016, American Chemical Society.

### 3.4. Solid-State Zn–Air Batteries

Solid-state Zn–air batteries with specific features of good stretchability, flexibility, and wearability can propel and accelerate the burgeoning next-generation portable electronics devices, such as flexible displays, electronic skin, and portable sensors.<sup>[138,139]</sup> Generally, KOH in poly(vinyl alcohol) (KOH-PVA) polymer electrolyte is used as the solid-state electrolyte in which PVA functions as the inert polymer matrix/host and KOH acts as ion conductors to fabricate all-solid-state Zn–air batteries.<sup>[7,118]</sup> Such polymer electrolyte is able to alleviate the electrolyte leakage and fabricate flexible batteries coupled with flexible electrodes.<sup>[138]</sup> To further improve the mechanical properties, a stretchable cross-linked poly(vinyl acetate)–poly(ethylene oxide)–KOH (PVA-PEO-KOH) hydrogel polymer electrolyte with a high ionic conductivity ( $0.3 \text{ S cm}^{-1}$ ) has been prepared, which can endure 300% maximal strain.<sup>[116]</sup> Incorporation of a cross-linker (e.g., glutaraldehyde) could further enhance the mechanical robustness.<sup>[118]</sup> Polyacrylic acid (PAA)-KOH electrolyte showed desirable mechanical robustness, good conductivity, and high degree of water retention.<sup>[8,140]</sup> In addition to polymer electrolyte, hydroxide conductive cellulose electrolyte membrane was also reported,<sup>[141]</sup> whose ionic conductivity was improved by functionalized GO and hydroxide conductive quaternary ammonium.<sup>[142]</sup>

Integrating a flexible oxygen electrode with a solid-state electrolyte membrane and a Zn electrode endows the promising construction of flexible Zn–air batteries. For instance, metal-free sulfur-modulated hierarchical  $\text{C}_2\text{N}$  aerogels ( $\text{S-C}_2\text{N}$ ) with a large specific surface area ( $1943 \text{ m}^2 \text{ g}^{-1}$ ) were used as bifunctional electrocatalysts for a flexible Zn–air battery (Figure 7a).<sup>[143]</sup> The air electrode was assembled by loading  $\text{S-C}_2\text{N}$  on mechanically flexible steel mesh. The Zn–air battery revealed a maximal power density of  $187 \text{ mW cm}^{-2}$  and high specific energy

densities of 695 and  $653 \text{ mAh g}^{-1}$  at 5 and  $50 \text{ mA cm}^{-2}$ , respectively (Figure 7b). The mechanical flexibility was further assessed by measuring the electrochemical performance under the bending, twisting, and stretching deformations, respectively. Remarkably, no obvious charge/discharge overpotential was observed in comparison with the flat configuration under different bending angles (Figure 7c), further confirming the excellent mechanical stability. In situ growing method was also adopted for the fabrication of flexible air electrode to avoid instability of additives such as polymer binders, decrease the interfacial resistance, and maximize the active sites simultaneously. As mentioned above, a carbon nanofiber (NCNF) network was introduced as binder-free freestanding air electrode to fabricate a flexible solid-state Zn–air battery (Figure 7d).<sup>[33]</sup> The 3D fibrous NCNF inherited and retained the structural integrity, high flexibility, and mechanical strength of electrospun polyimide. The flexible Zn–air battery (Figure 7e) exhibited a high discharge voltage of 1.0 V and a low charge voltage of 1.78 V at  $2 \text{ mA cm}^{-2}$ . As shown in Figure 7f, even under stringent bending condition, the charge and discharge potentials revealed negligible change. Besides, the aforesaid defect-rich graphene on carbon cloth surface was used as a freestanding bifunctional air electrode,<sup>[130]</sup> and a stable cycling under bending was demonstrated.

## 4. Carbon Electrocatalysts for Li–Air Batteries

The Li–air battery is another highly promising energy device due to the large theoretical energy density as high as  $\approx 3842 \text{ mAh g}^{-1}$ .<sup>[144]</sup> Oxygen electrochemistry is also the key to determine the final battery performances. Huge advances have been achieved for assembling such batteries with various air electrodes and in-depth understanding of the basic energy storage

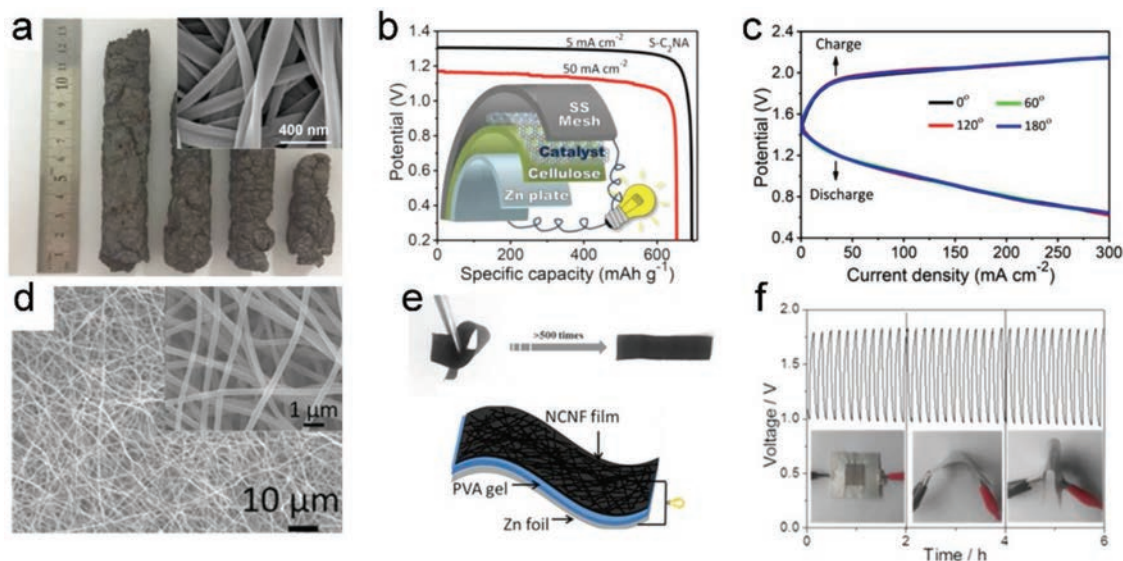


**Figure 7.** a) Digital image of 3D holey S-C<sub>2</sub>N aerogel; inset displays the SEM images. b) Specific capacity of a flexible Zn–air battery at current density of 5 and 50 mA cm<sup>-2</sup>, inset reveals the schematic representation of the solid Zn–air battery. c) Charge and discharge polarization curves as a function of bending angles. a) Adapted with permission.<sup>[143]</sup> Copyright 2018, American Chemical Society. b,c) Reproduced with permission.<sup>[143]</sup> Copyright 2018, American Chemical Society. d) SEM image of NCNF at different magnification. e) Flexible demonstration of NCNF after 500 times bending and schematic diagram of a flexible Zn–air battery. f) Galvanostatic discharge–charge curves at 2 mA cm<sup>-2</sup>. d) Adapted with permission.<sup>[33]</sup> Copyright 2016, Wiley-VCH. e,f) Reproduced with permission.<sup>[33]</sup> Copyright 2016, Wiley-VCH.

mechanisms. However, the impurity of ambient air (e.g., CO<sub>2</sub>, H<sub>2</sub>O, N<sub>2</sub>) typically results in side reactions with the formation of the irreversible byproducts for large polarization and severe degradation of battery performance.<sup>[145]</sup> Therefore, extensive researches have been performed on the basis of Li–O<sub>2</sub> systems.

**Figure 8a** presents the typical structure of a Li–O<sub>2</sub> battery, in which the porous catalyst as the air electrode and Li foil as the counter electrode are assembled with a nonaqueous electrolyte soaking separator between them.<sup>[5b]</sup> It operates through ORR with the formation of Li<sub>2</sub>O<sub>2</sub> in the discharging process and OER with the reversible decomposition of Li<sub>2</sub>O<sub>2</sub> in the charge process. Bruce and co-workers<sup>[5b]</sup> reported that the electrolyte is crucial to the nucleation process of Li<sub>2</sub>O<sub>2</sub>, and the donor number (DN) of the solvent largely affected the oxygen reduction pathways (Figure 8b). Through the solution pathway in high-DN solvents, electrochemical reactions on the cathode with dissolution of intermediate product (LiO<sub>2</sub>) generate the large particles of Li<sub>2</sub>O<sub>2</sub> afterward, leading to superior electrochemical activity. In contrast, low-DN solvents contribute the surface pathway with LiO<sub>2</sub> deposition on the electrode surface, which induced the growth of Li<sub>2</sub>O<sub>2</sub> film and poor battery performance.

Hierarchically porous structure is also extremely essential for promoting the catalytic property of the air electrode materials. As proposed by Wang and co-workers in Figure 8c, both pore size and wall density with different specific surface areas of the 3D ordered mesoporous (3DOM) carbons determine Li<sub>2</sub>O<sub>2</sub> formation and decomposition with the accumulation of the byproducts, thus leading to different battery performances (Figure 8d,e).<sup>[146]</sup> Similar conclusion was drawn from the research on the air electrodes containing 3D ordered mesoporous/macroporous carbon sphere arrays (MMCSAs) in Figure 8f.<sup>[147]</sup> The mesopores are helpful for electrolyte wetting and boosting the Li<sup>+</sup> diffusion and e<sup>-</sup> transport while

macropores offer abundant tunnels for oxygen diffusion and enough space for storing Li<sub>2</sub>O<sub>2</sub>. Thanks to the unique architecture, the MMCSAs delivered remarkably better discharge specific capacities and cycling performance (Figure 8g,h).

To optimize the electrocatalytic activity of the metal-free carbon for Li–O<sub>2</sub> batteries, vertically aligned nitrogen-doped coral-like carbon nanofiber (VA-NCCF) arrays were synthesized by CVD growth.<sup>[148]</sup> The zigzag-like carbon fibers on a Si wafer aligned and slightly tangled together, which offers extraordinary conductivity for both the in-plane and vertical directions. This provides vast channels for efficient reaction mass movement. Li<sub>2</sub>O<sub>2</sub> could densely deposit along the VA-NCCF in the discharge processes, and almost disappear in the charge processes. Therefore, the VA-NCCF cathode exhibits low overpotentials and a high reversibility with a specific capacity of 1000 mAh g<sup>-1</sup> at different current densities. Its electrocatalytic performance is much better than those of the CNT and VA-CNT cathodes. Moreover, a specific capacity of about 40 000 mAh g<sup>-1</sup> was reversibly achieved for the VA-NCCF cathode within 2.2–4.4 V at a current density of 50 mA g<sup>-1</sup>. Furthermore, the VA-NCCF cathode was repeatedly cycled for over 150 cycles with lower initial overpotentials. Dai and co-workers<sup>[149]</sup> reported that a holey graphene (hG) disc was used as the air electrode to fabricate Li–O<sub>2</sub> batteries (**Figure 9a**). The hG disc was constructed by dry compressibility related to in-plane holes on their surface without using solvent and binder. The hG cathode (5 mg cm<sup>-2</sup>) delivered an ultrahigh areal capacity of about 40 mAh cm<sup>-2</sup> at 0.2 mA cm<sup>-2</sup> (Figure 9b). The discharge product Li<sub>2</sub>O<sub>2</sub> preferentially accumulates on the air side with a gradient into the inner space of cathode, which renders more Li<sub>2</sub>O<sub>2</sub> storage and larger capacity. It is highly promising to enhance the cathode performance of practical Li–O<sub>2</sub> batteries by using the freestanding hG.

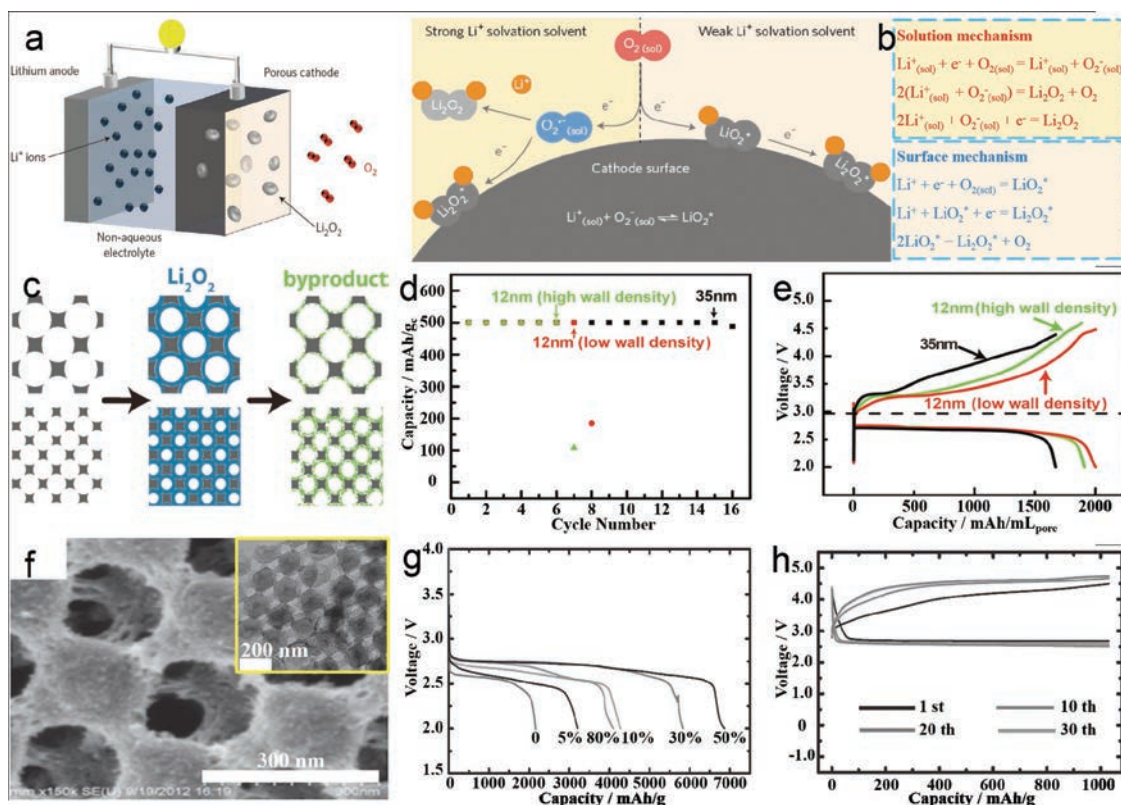


**Figure 8.** a,b) Schematic representation of a nonaqueous Li–O<sub>2</sub> battery with corresponding oxygen electrochemical reactions. a,b) Reproduced with permission.<sup>[5b]</sup> Copyright 2016, Nature Publishing Group. c) Illustration of reaction products in 3DOM carbons with different pore structures. d,e) Electrochemical performance of 3DOM carbons. c–e) Reproduced with permission.<sup>[146]</sup> Copyright 2015, Wiley-VCH. f) Morphology of the MMCSAs. g) Battery performance using different amount of the MMCSAs and h) 30 wt% MMCSAs. f,h) Reproduced with permission.<sup>[147]</sup> Copyright 2013, Wiley-VCH. g) Reproduced with permission.<sup>[147]</sup> Copyright 2013, Wiley-VCH.

By thermally annealing hGr under air and NH<sub>3</sub> atmosphere successively, a low-cost and efficient N-doped holey graphene (N-HGr) was achieved and used to fabricate Li–O<sub>2</sub> batteries.<sup>[77]</sup> Figure 9c shows the initial polarization curves of the N-HGr electrode with a specific capacity of 800 mAh g<sup>−1</sup> at 40 mA g<sup>−1</sup>. The potential platforms are 2.93 and 3.47 V, respectively, leading to a high round-trip efficiency of 85%. Its repeated terminal voltages in Figure 9d are changeless after more than 60 cycles, while the r-Gr electrode exhibits a poor cycling stability of 30 cycles in Figure 9e. The N-HGr electrode (Figure 9f) delivers remarkable discharge/charge capacities of around 17 000 mAh g<sup>−1</sup> within 2.2–4.4 V at 100 mA g<sup>−1</sup>. The N-HGr electrode exhibited superior electrocatalytic activity in comparison to the r-Gr electrode and the reported composite electrodes containing transition metal oxides or precious metals under similar testing condition.<sup>[77]</sup> This is ascribed to the fancy structure of the r-Gr electrode (Figure 9g): The holes on its surface are beneficial for rapidly transporting Li<sup>+</sup> ions and O<sub>2</sub>, leading to the reversible redox reactions of Li<sub>2</sub>O<sub>2</sub>; the defects on its planes act as active catalytic sites to promote both ORR and OER via metal-free electrocatalysis, resulting in excellent battery performance.

## 5. Conclusions and Perspectives

The plentiful research and remarkable advances on the carbon electrocatalysts have been achieved along with the deep

understanding on the basic catalytic mechanisms and the rapid development of advanced characterization techniques to reveal the intrinsic active sites for oxygen reduction and evolution reactions. Consequently, metal–air batteries (e.g., Zn–air and Li–air batteries) were boosted on the basis of the rational design of advanced bifunctional carbon electrocatalysts via the atomic modulation and optimal structure design. This research progress summarizes the recent advances on the fundamental understanding on the electrocatalytic mechanism of carbon materials for ORR/OER, the regulation strategies, and execution modes over active sites, the fabrication of integrated/flexible electrodes, and the configuration and operation of metal–air batteries. For further advancement of carbon-based catalysts toward applications in metal–air batteries, the specific issues are listed as follows:

There are still significant gaps between ex situ characterization/computation-derived activity prediction and the practical description of an electrocatalyst in three-electrode tests. Thus, advanced techniques such as spherical aberration electron microscopy, in situ or operando photoelectron spectroscopy, and X-ray absorption spectroscopy are requested to identify the real active sites of metal-free carbon catalysts, aimed to feasible design on highly efficient ORR/OER electrocatalysts for metal–air batteries. Additionally, the influences of other factors, for example, electrolyte, catalyst loading, atmospheric pressure, current densities, and operating temperatures,<sup>[7,68]</sup> should also

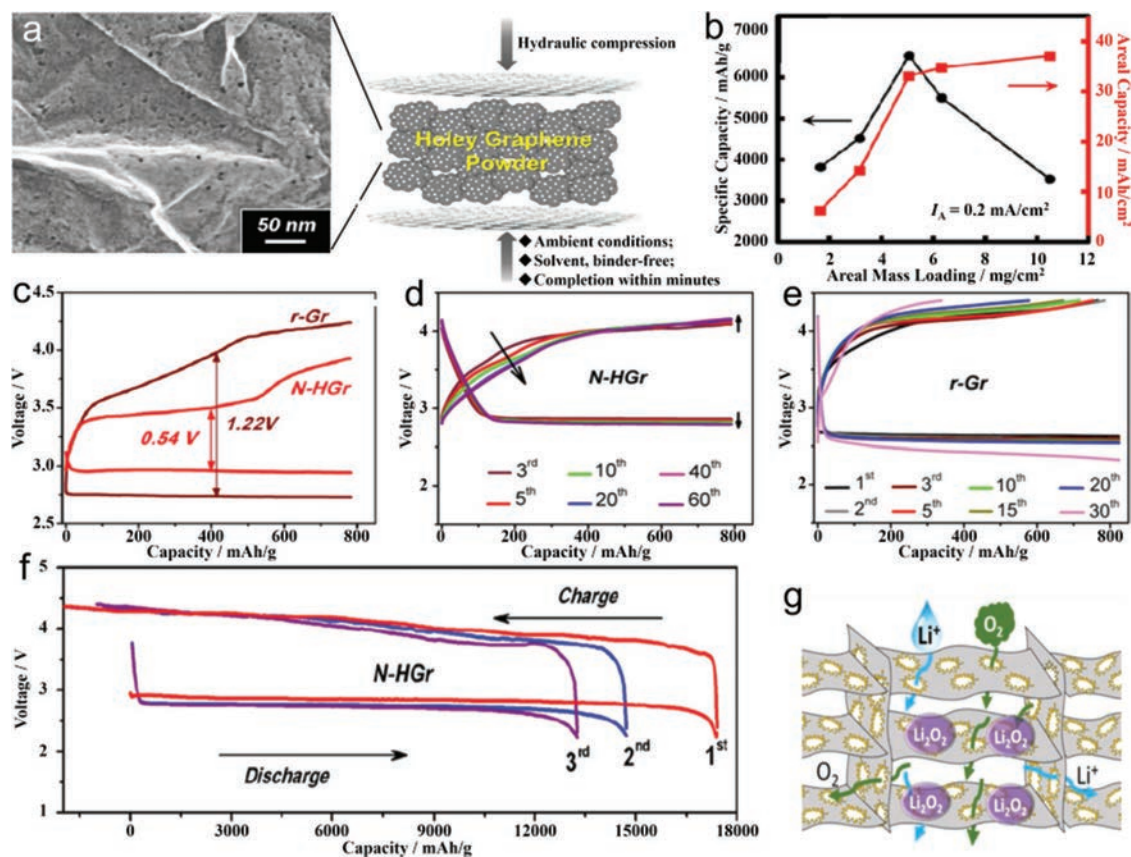


**Figure 9.** a) SEM image of freestanding hG electrode made by hydraulic compression. b) Specific capacities and areal capacities of the hG electrodes based on areal mass loading. a,b) Reproduced with permission.<sup>[149]</sup> Copyright 2017, American Chemical Society. c) Initial and d,e) typical discharge/charge curves of N-HGr electrode with a fixed capacity of 800 mAh g<sup>-1</sup>. f) Discharge/charge profiles of N-HGr electrode within 2.2–4.4 V. g) Schematic illustration of reactions on N-HGr electrode. c–g) Reproduced with permission.<sup>[177]</sup> Copyright 2016, American Chemical Society.

be analyzed and unified to form universal principles for reasonably evaluating the catalytic performance.

The optimization of synthetic strategies is efficient to regulate the highly active/stable sites toward the practical applications of carbon bifunctional electrocatalysts in metal–air batteries. It is highly critical to adopt an efficient but always suitable synthetic approach to combine the most favorable factors customized for specific applications in metal–air batteries. For instance, there should be some significant difference in the design of pore structure, active sites, surface hydrophilia/hydrophobicity, etc., when aiming at rechargeable Li–air batteries and primary Zn–air batteries. An adopted synthesis with cost-effective and eco-friendly features, efficient mono-/bifunctionality of the targeted catalysts, porosity configuration of the electrode, high scalability and tailorability for the air electrode are requested.

Advanced air electrode design by directly growing carbon-based catalysts onto the bendable carbon/metal substrates is highly desired, especially for flexible metal–air batteries. It can not only avoid the tedious air electrode preparation, but also be free of the use of ancillary materials for full exposure of more active sites and pores. New facile strategies for fabrication of such integrated air electrodes are requisite. Additionally, it is still a huge challenge to overcome the degradation of metal-free carbon-based electrocatalysts under the harsh oxidative

conditions. It is thus imperative to understand the degradation mechanism, and to develop highly corrosion-resistant carbon-based air electrode. To this end, in situ spectrum technology on the operational metal–air battery is a potential tool to analyze the degradation mechanism for raising a feasible route to tackle the stability issue.

Along with the recent achievements and increasing research in metal-free carbon electrocatalysts for metal–air batteries, this field is demonstrated to be prosperous with broad prospects. Accelerated research and development of relevant technologies to overcome the extant insufficiency are highly encouraged. Overall, the carbon-based catalysts are approaching practical applications in metal–air batteries propelled with mass of progress, which we believe, could also be applied to other fields of electrochemical energy systems in view of the continuous interest worldwide. We expect this progress could provide profound understanding and inspiration on the design of advanced carbon catalysts from material synthesis to energy conversion device applications.

## Acknowledgements

Y.H., Y.W., and C.T. contributed equally to this work. This work was supported by the Natural Scientific Foundation of China (21503116), National Key Research and Development Program (2016YFA0202500,

2016YFA0200101, and 2015CB932500), Taishan Scholars Program of Shandong Province (tsqn20161004), and the Youth 1000 Talent Program of China.

## Conflict of Interest

The authors declare no conflict of interest.

## Keywords

bifunctional electrocatalysts, metal–air batteries, metal-free carbon, oxygen evolution reaction, oxygen reduction reaction

Received: June 15, 2018

Revised: July 14, 2018

Published online: September 24, 2018

- [1] Z. Yang, J. Zhang, M. C. Kintner-Meyer, X. Lu, D. Choi, J. P. Lemmon, J. Liu, *Chem. Rev.* **2011**, *111*, 3577.
- [2] P. C. Stern, B. K. Sovacool, T. Dietz, *Nat. Clim. Change* **2016**, *6*, 547.
- [3] a) M. S. Dresselhaus, I. L. Thomas, *Nature* **2001**, *414*, 332; b) S. Chu, Y. Cui, N. Liu, *Nat. Mater.* **2016**, *16*, 16; c) H. J. Peng, J. Q. Huang, X. B. Cheng, Q. Zhang, *Adv. Energy Mater.* **2017**, *7*, 1700260.
- [4] a) Z. W. Seh, J. Kibsgaard, C. F. Dickens, I. Chorkendorff, J. K. Nørskov, T. F. Jaramillo, *Science* **2017**, *355*, eaad4998; b) X. Md. Arafat Rahman, C. Wen, *J. Electrochem. Soc.* **2013**, *160*, A1759; c) X. Ren, Y. Wu, *J. Am. Chem. Soc.* **2013**, *135*, 2923; d) P. Hartmann, C. L. Bender, M. Vracar, A. K. Durr, A. Garsuch, J. Janek, P. Adelhelm, *Nat. Mater.* **2013**, *12*, 228.
- [5] a) I. Roger, M. A. Shipman, M. D. Symes, *Nat. Rev. Chem.* **2017**, *1*, 0003; b) D. Aurbach, B. D. McCloskey, L. F. Nazar, P. G. Bruce, *Nat. Energy* **2016**, *1*, 16128.
- [6] J. Song, B. Wu, Z. Zhou, G. Zhu, Y. Liu, Z. Yang, L. Lin, G. Yu, F. Zhang, G. Zhang, H. Duan, G. D. Stucky, X. Chen, *Angew. Chem., Int. Ed.* **2017**, *56*, 8110.
- [7] J. Fu, Z. P. Cano, M. G. Park, A. Yu, M. Fowler, Z. Chen, *Adv. Mater.* **2017**, *29*, 1604685.
- [8] A. Sumboja, M. Lübke, Y. Wang, T. An, Y. Zong, Z. Liu, *Adv. Energy Mater.* **2017**, *7*, 1700927.
- [9] H. Wu, X. Jiang, Y. Ye, C. Yan, S. Xie, S. Miao, G. Wang, X. Bao, *J. Energy Chem.* **2017**, *26*, 1181.
- [10] Z. Zhao, M. Li, L. Zhang, L. Dai, Z. Xia, *Adv. Mater.* **2015**, *27*, 6834.
- [11] X. Liu, L. Dai, *Nat. Rev. Mater.* **2016**, *1*, 16064.
- [12] X. Zhang, X. Cheng, Q. Zhang, *J. Energy Chem.* **2016**, *25*, 967.
- [13] C. Hu, X. Chen, Q. Dai, M. Wang, L. Qu, L. Dai, *Nano Energy* **2017**, *41*, 367.
- [14] A. Mulyadi, Z. Zhang, M. Dutzer, W. Liu, Y. Deng, *Nano Energy* **2017**, *32*, 336.
- [15] G. C. da Silva, M. R. Fernandes, E. A. Ticianelli, *ACS Catal.* **2018**, *8*, 2081.
- [16] a) J. Zhang, C. Guo, L. Zhang, C. M. Li, *Chem. Commun.* **2013**, *49*, 6334; b) L. Wang, C. Yang, S. Dou, S. Wang, J. Zhang, X. Gao, J. Ma, Y. Yu, *Electrochim. Acta* **2016**, *219*, 592.
- [17] F. D. K. Gong, Z. Xia, M. Durstock, L. Dai, *Science* **2009**, *323*, 760.
- [18] J. Zhang, Z. Zhao, Z. Xia, L. Dai, *Nat. Nanotechnol.* **2015**, *10*, 444.
- [19] a) Y. Jiao, Y. Zheng, M. Jaroniec, S. Z. Qiao, *Chem. Soc. Rev.* **2015**, *44*, 2060; b) X. K. Kong, C. L. Chen, Q. W. Chen, *Chem. Soc. Rev.* **2014**, *43*, 2841.
- [20] L. Dai, Y. Xue, L. Qu, H. J. Choi, J. B. Baek, *Chem. Rev.* **2015**, *115*, 4823.
- [21] Z. X. Pei, J. X. Zhao, Y. Huang, Y. Huang, M. S. Zhu, Z. F. Wang, Z. F. Chen, C. Y. Zhi, *J. Mater. Chem. A* **2016**, *4*, 12205.
- [22] J. Duan, S. Chen, M. Jaroniec, S. Z. Qiao, *ACS Catal.* **2015**, *5*, 5207.
- [23] L. Dai, *Nat. Energy* **2016**, *1*, 16041.
- [24] a) Z. Xiang, Q. Dai, J. F. Chen, L. Dai, *Adv. Mater.* **2016**, *28*, 6253; b) C. Tang, M.-M. Titirici, Q. Zhang, *J. Energy Chem.* **2017**, *26*, 1077.
- [25] a) X. Zhao, X. Zou, X. Yan, C. L. Brown, Z. Chen, G. Zhu, X. Yao, *Inorg. Chem. Front.* **2016**, *3*, 417; b) D. Yan, Y. Li, J. Huo, R. Chen, L. Dai, S. Wang, *Adv. Mater.* **2017**, *29*, 1906459; c) H. B. Yang, J. Miao, S.-F. Hung, J. Chen, H. B. Tao, X. Wang, L. Zhang, R. Chen, J. Gao, H. M. Chen, L. Dai, B. Liu, *Sci. Adv.* **2016**, *2*, e1501122.
- [26] a) D. Liu, L. I. Tao, D. Yan, Y. Zou, S. Wang, *ChemElectroChem.* **2018**, *5*, 1; b) B. Men, Y. Sun, M. Li, C. Hu, M. Zhang, L. Wang, Y. Tang, Y. Chen, P. Wan, J. Pan, *ACS Appl. Mater. Interfaces* **2016**, *8*, 1415; c) T. Zhou, Y. Zhou, R. Ma, Z. Zhou, G. Liu, Q. Liu, Y. Zhu, J. Wang, *Carbon* **2017**, *114*, 177.
- [27] W. Niu, L. Li, X. Liu, N. Wang, J. Liu, W. Zhou, Z. Tang, S. Chen, *J. Am. Chem. Soc.* **2015**, *137*, 5555.
- [28] D. J. Yang, L. J. Zhang, X. C. Yan, X. D. Yao, *Small Methods* **2017**, *1*, 1700209.
- [29] C. Tang, H. F. Wang, Q. Zhang, *Acc. Chem. Res.* **2018**, *51*, 881.
- [30] a) D. W. Wang, D. S. Su, *Energy Environ. Sci.* **2014**, *7*, 576; b) Y. Jiao, Y. Zheng, M. Jaroniec, S. Z. Qiao, *J. Am. Chem. Soc.* **2014**, *136*, 4394.
- [31] K. P. Gong, F. Du, Z. H. Xia, M. Durstock, L. M. Dai, *Science* **2009**, *323*, 760.
- [32] a) L. Zhang, Z. Xia, *J. Phys. Chem. C* **2011**, *115*, 11170; b) D. Guo, R. Shibuya, C. Akiba, S. Saji, T. Kondo, J. Nakamura, *Science* **2016**, *351*, 361; c) W. Ding, L. Li, K. Xiong, Y. Wang, W. Li, Y. Nie, S. G. Chen, X. Q. Qi, Z. D. Wei, *J. Am. Chem. Soc.* **2015**, *137*, 5414.
- [33] Q. Liu, Y. Wang, L. Dai, J. Yao, *Adv. Mater.* **2016**, *28*, 3000.
- [34] a) D. S. Geng, Y. Chen, Y. G. Chen, Y. L. Li, R. Y. Li, X. L. Sun, S. Y. Ye, S. Knights, *Energy Environ. Sci.* **2011**, *4*, 760; b) Z. Y. Lin, G. H. Waller, Y. Liu, M. L. Liu, C. P. Wong, *Carbon* **2013**, *53*, 130.
- [35] Z. X. Pei, H. F. Li, Y. Huang, Q. Xue, Y. Huang, M. S. Zhu, Z. F. Wang, C. Y. Zhi, *Energy Environ. Sci.* **2017**, *10*, 742.
- [36] G. L. Tian, Q. Zhang, B. Zhang, Y. G. Jin, J. Q. Huang, D. S. Su, F. Wei, *Adv. Funct. Mater.* **2014**, *24*, 5956.
- [37] Z. Zhao, Z. Xia, *ACS Catal.* **2016**, *6*, 1553.
- [38] S. Dou, A. Shen, L. Tao, S. Wang, *Chem. Commun.* **2014**, *50*, 10672.
- [39] S. Wang, D. Yu, L. Dai, *J. Am. Chem. Soc.* **2011**, *133*, 5182.
- [40] I.-Y. Jeon, S. Zhang, L. Zhang, H.-J. Choi, J.-M. Seo, Z. Xia, L. Dai, J.-B. Baek, *Adv. Mater.* **2013**, *25*, 6138.
- [41] L. Zhang, J. Niu, M. Li, Z. Xia, *J. Phys. Chem. C* **2014**, *118*, 3545.
- [42] J. Liang, Y. Jiao, M. Jaroniec, S. Z. Qiao, *Angew. Chem., Int. Ed.* **2012**, *51*, 11496.
- [43] Z. K. Kou, B. B. Guo, D. P. He, J. Zhang, S. C. Mu, *ACS Energy Lett.* **2018**, *3*, 184.
- [44] Y. Zhao, R. Nakamura, K. Kamiya, S. Nakanishi, K. Hashimoto, *Nat. Commun.* **2013**, *4*, 2390.
- [45] X. Y. Lu, W. L. Yim, B. H. R. Suryanto, C. Zhao, *J. Am. Chem. Soc.* **2015**, *137*, 2901.
- [46] L. Li, H. Yang, J. Miao, L. Zhang, H.-Y. Wang, Z. Zeng, W. Huang, X. Dong, B. Liu, *ACS Energy Lett.* **2017**, *2*, 294.
- [47] A. M. El-Sawy, I. M. Mosa, D. Su, C. J. Guild, S. Khalid, R. Joesten, J. F. Rusling, S. L. Suib, *Adv. Energy Mater.* **2016**, *6*, 1501966.
- [48] Y. Zhang, X. L. Fan, J. H. Jian, D. S. Yu, Z. S. Zhang, L. M. Dai, *Energy Environ. Sci.* **2017**, *10*, 2312.
- [49] G. Wu, A. Santandreu, W. Kellogg, S. Gupta, O. Ogoke, H. G. Zhang, H. L. Wang, L. M. Dai, *Nano Energy* **2016**, *29*, 83.

- [50] K. Zhou, B. Li, Q. Zhang, J. Q. Huang, G. L. Tian, J. C. Jia, M. Q. Zhao, G. H. Luo, D. S. Su, F. Wei, *ChemSusChem* **2014**, *7*, 723.
- [51] a) S. Y. Wang, L. P. Zhang, Z. H. Xia, A. Roy, D. W. Chang, J. B. Baek, L. M. Dai, *Angew. Chem., Int. Ed.* **2012**, *51*, 4209; b) Y. Zhang, X. D. Zhuang, Y. Z. Su, F. Zhang, X. L. Feng, *J. Mater. Chem. A* **2014**, *2*, 7742.
- [52] Y. Zheng, Y. Jiao, L. Ge, M. Jaroniec, S. Z. Qiao, *Angew. Chem., Int. Ed.* **2013**, *52*, 3110.
- [53] J. Zhang, L. Qu, G. Shi, J. Liu, J. Chen, L. Dai, *Angew. Chem., Int. Ed.* **2016**, *55*, 2230.
- [54] S. Chen, J. J. Duan, M. Jaroniec, S. Z. Qiao, *Adv. Mater.* **2014**, *26*, 2925.
- [55] Y. P. Zhu, Y. Jing, A. Vasileff, T. Heine, S. Z. Qiao, *Adv. Energy Mater.* **2017**, *7*, 1602928.
- [56] J. Zhao, Y. Liu, X. Quan, S. Chen, H. Zhao, H. Yu, *Electrochim. Acta* **2016**, *204*, 169.
- [57] C. Tang, H.-F. Wang, X. Chen, B.-Q. Li, T.-Z. Hou, B. Zhang, Q. Zhang, M.-M. Titirici, F. Wei, *Adv. Mater.* **2016**, *28*, 6845.
- [58] Y. Jiang, L. Yang, T. Sun, J. Zhao, Z. Lyu, O. Zhuo, X. Wang, Q. Wu, J. Ma, Z. Hu, *ACS Catal.* **2015**, *5*, 6707.
- [59] L. Zhang, Q. Xu, J. Niu, Z. Xia, *Phys. Chem. Chem. Phys.* **2015**, *17*, 16733.
- [60] Y. Jia, L. Z. Zhang, A. J. Du, G. P. Gao, J. Chen, X. C. Yan, C. L. Brown, X. D. Yao, *Adv. Mater.* **2016**, *28*, 9532.
- [61] Y. Ito, Y. H. Shen, D. Hojo, Y. Itagaki, T. Fujita, L. H. Chen, T. Aida, Z. Tang, T. Adschiri, M. W. Chen, *Adv. Mater.* **2016**, *28*, 10644.
- [62] R. Li, Z. Wei, X. Gou, *ACS Catal.* **2015**, *5*, 4133.
- [63] J. T. Zhang, L. M. Dai, *Angew. Chem., Int. Ed.* **2016**, *55*, 13296.
- [64] K. Qu, Y. Zheng, S. Dai, S. Z. Qiao, *Nano Energy* **2016**, *19*, 373.
- [65] a) X. Mao, T. A. Hatton, *Ind. Eng. Chem. Res.* **2015**, *54*, 4033; b) X. Gao, L. Wang, J. Ma, Y. Wang, J. Zhang, *Inorg. Chem. Front.* **2017**, *4*, 1582.
- [66] Y. Ito, H. J. Qiu, T. Fujita, Y. Tanabe, K. Tanigaki, M. W. Chen, *Adv. Mater.* **2014**, *26*, 4145.
- [67] a) G. L. Tian, M. Q. Zhao, D. S. Yu, X. Y. Kong, J. Q. Huang, Q. Zhang, F. Wei, *Small* **2014**, *10*, 2251; b) T. Y. Ma, S. Dai, M. Jaroniec, S. Z. Qiao, *Angew. Chem., Int. Ed.* **2014**, *53*, 7281.
- [68] M. Qiao, C. Tang, L. C. Tanase, C. M. Teodorescu, C. Chen, Q. Zhang, M.-M. Titirici, *Mater. Horiz.* **2017**, *4*, 895.
- [69] K. Ding, Q. Liu, Y. Bu, Y. Huang, J. Lv, J. Wu, S. C. Abbas, Y. Wang, *RSC Adv.* **2016**, *6*, 93318.
- [70] a) X. W. Yu, M. Zhang, J. Chen, Y. R. Li, G. Q. Shi, *Adv. Energy Mater.* **2016**, *6*, 1501492; b) Q. Liu, Y. B. Wang, L. M. Dai, J. N. Yao, *Adv. Mater.* **2016**, *28*, 3000.
- [71] Y. Huang, P. Wu, Y. Wang, W. Wang, D. Yuan, J. Yao, *J. Mater. Chem. A* **2014**, *2*, 19765.
- [72] J. Zhang, C. Zhang, Y. Zhao, I. S. Amiinu, H. Zhou, X. Liu, Y. Tang, S. Mu, *Appl. Catal., B* **2017**, *211*, 148.
- [73] D. Gu, R. Ma, Y. Zhou, F. Wang, K. Yan, Q. Liu, J. Wang, *ACS Sustainable Chem. Eng.* **2017**, *5*, 11105.
- [74] H.-W. Liang, Z.-Y. Wu, L.-F. Chen, C. Li, S.-H. Yu, *Nano Energy* **2015**, *11*, 366.
- [75] S. Chen, J. Duan, M. Jaroniec, S. Z. Qiao, *Adv. Mater.* **2014**, *26*, 2925.
- [76] G. L. Tian, M. Q. Zhao, D. Yu, X. Y. Kong, J. Q. Huang, Q. Zhang, F. Wei, *Small* **2014**, *10*, 2251.
- [77] J. Shui, Y. Lin, J. W. Connell, J. Xu, X. Fan, L. Dai, *ACS Energy Lett.* **2016**, *1*, 260.
- [78] a) W. J. Jiang, S. Niu, T. Tang, Q. H. Zhang, X. Z. Liu, Y. Zhang, Y. Y. Chen, J. H. Li, L. Gu, L. J. Wan, J. S. Hu, *Angew. Chem., Int. Ed.* **2017**, *56*, 6572; b) S. Chen, J. Duan, J. Ran, S. Z. Qiao, *Adv. Sci.* **2015**, *2*, 1400015.
- [79] B. Bayatsarmadi, Y. Zheng, M. Jaroniec, S. Z. Qiao, *Chem. Asian J.* **2015**, *10*, 1546.
- [80] H. Yu, L. Shang, T. Bian, R. Shi, G. I. Waterhouse, Y. Zhao, C. Zhou, L. Z. Wu, C. H. Tung, T. Zhang, *Adv. Mater.* **2016**, *28*, 5080.
- [81] K. Qu, Y. Zheng, S. Dai, S. Z. Qiao, *Nanoscale* **2015**, *7*, 12598.
- [82] L.-T. Song, Z.-Y. Wu, H.-W. Liang, F. Zhou, Z.-Y. Yu, L. Xu, Z. Pan, S.-H. Yu, *Nano Energy* **2016**, *19*, 117.
- [83] G. Wang, Y. Sun, D. Li, H. W. Liang, R. Dong, X. Feng, K. Mullen, *Angew. Chem., Int. Ed.* **2015**, *54*, 15191.
- [84] Z. Pei, H. Li, Y. Huang, Q. Xue, Y. Huang, M. Zhu, Z. Wang, C. Zhi, *Energy Environ. Sci.* **2017**, *10*, 742.
- [85] I. S. Amiinu, J. Zhang, Z. Kou, X. Liu, O. K. Asare, H. Zhou, K. Cheng, H. Zhang, L. Mai, M. Pan, S. Mu, *ACS Appl. Mater. Interfaces* **2016**, *8*, 29408.
- [86] J. Zhang, H. Zhou, J. Zhu, P. Hu, C. Hang, J. Yang, T. Peng, S. Mu, Y. Huang, *ACS Appl. Mater. Interfaces* **2017**, *9*, 24545.
- [87] S. Chen, J. Duan, Y. Zheng, X. Chen, X. W. Du, M. Jaroniec, S.-Z. Qiao, *Energy Storage Mater.* **2015**, *1*, 17.
- [88] C. Dong, T. Kou, H. Gao, Z. Peng, Z. Zhang, *Adv. Energy Mater.* **2018**, *8*, 1701347.
- [89] C. Tang, H. F. Wang, X. Chen, B. Q. Li, T. Z. Hou, B. Zhang, Q. Zhang, M. M. Titirici, F. Wei, *Adv. Mater.* **2016**, *28*, 6845.
- [90] C. Hu, L. Dai, *Adv. Mater.* **2017**, *29*, 1604942.
- [91] Y. Jia, L. Zhang, A. Du, G. Gao, J. Chen, X. Yan, C. L. Brown, X. Yao, *Adv. Mater.* **2016**, *28*, 9532.
- [92] Z. Xiao, X. Huang, L. Xu, D. Yan, J. Huo, S. Wang, *Chem. Commun.* **2016**, *52*, 13008.
- [93] Y. Xue, H. Chen, J. Qu, L. Dai, *2D Mater.* **2015**, *2*, 044001.
- [94] L. Tao, Q. Wang, S. Dou, Z. Ma, J. Huo, S. Wang, L. Dai, *Chem. Commun.* **2016**, *52*, 2764.
- [95] a) Z. Kou, B. Guo, D. He, J. Zhang, S. Mu, *ACS Energy Lett.* **2017**, *3*, 184; b) Z. Pei, J. Zhao, Y. Huang, Y. Huang, M. Zhu, Z. Wang, Z. Chen, C. Zhi, *J. Mater. Chem. A* **2016**, *4*, 12205.
- [96] S. C. Abbas, K. Ding, Q. Liu, Y. Huang, Y. Bu, J. Wu, J. Lv, M. A. Ghausi, Y. Wang, *J. Mater. Chem. A* **2016**, *4*, 7924.
- [97] J. Zhu, H. Zhou, C. Zhang, J. Zhang, S. Mu, *Nanoscale* **2017**, *9*, 13257.
- [98] Y. Wang, L. Tao, Z. Xiao, R. Chen, Z. Jiang, S. Wang, *Adv. Funct. Mater.* **2018**, *11*, 1705356.
- [99] Y. Zhao, S. Huang, M. Xia, S. Rehman, S. Mu, Z. Kou, Z. Zhang, Z. Chen, F. Gao, Y. Hou, *Nano Energy* **2016**, *28*, 346.
- [100] K. Abraham, Z. Jiang, *J. Electrochem. Soc.* **1996**, *143*, 1.
- [101] Q. Sun, H. Yadegari, M. N. Banis, J. Liu, B. Xiao, B. Wang, S. Lawes, X. Li, R. Li, X. Sun, *Nano Energy* **2015**, *12*, 698.
- [102] Y. Li, H. Yadegari, X. Li, M. N. Banis, R. Li, X. Sun, *Chem. Commun.* **2013**, *49*, 11731.
- [103] B. Sun, K. Kretschmer, X. Xie, P. Munroe, Z. Peng, G. Wang, *Adv. Mater.* **2017**, *29*, 1606816.
- [104] a) H. Yadegari, M. N. Banis, B. Xiao, Q. Sun, X. Li, A. Lushington, B. Wang, R. Li, T.-K. Sham, X. Cui, *Chem. Mater.* **2015**, *27*, 3040; b) Z. Jian, Y. Chen, F. Li, T. Zhang, C. Liu, H. Zhou, *J. Power Sources* **2014**, *251*, 466.
- [105] H. Wang, C. Tang, Q. Zhang, *Adv. Funct. Mater.* **2018**, *28*, 1803329.
- [106] Z. Liu, Z. Zhao, Y. Wang, S. Dou, D. Yan, D. Liu, Z. Xia, S. Wang, *Adv. Mater.* **2017**, *29*, 1606207.
- [107] J. Zhang, Z. Xia, L. Dai, *Sci. Adv.* **2015**, *1*, e1500564.
- [108] Y. Li, H. Dai, *Chem. Soc. Rev.* **2014**, *43*, 5257.
- [109] a) P. Gu, M. Zheng, Q. Zhao, X. Xiao, H. Xue, H. Pang, *J. Mater. Chem. A* **2017**, *5*, 7651; b) J.-S. Lee, S. T. Kim, R. Cao, N.-S. Choi, M. Liu, K. T. Lee, J. Cho, *Adv. Energy Mater.* **2011**, *1*, 34.
- [110] A. R. Mainar, O. Leonet, M. Bengoechea, I. Boyano, I. de Meatza, A. Kvasha, A. Guerfi, J. A. Blázquez, *Int. J. Energy Res.* **2016**, *40*, 1032.
- [111] X. Liu, M. Park, M. G. Kim, S. Gupta, G. Wu, J. Cho, *Angew. Chem., Int. Ed.* **2015**, *54*, 9654.

- [112] Y. Su, Z. Yao, F. Zhang, H. Wang, Z. Mics, E. Cánovas, M. Bonn, X. Zhuang, X. Feng, *Adv. Funct. Mater.* **2016**, 26, 5893.
- [113] P. Arora, Z. J. Zhang, *Chem. Rev.* **2004**, 104, 4419.
- [114] T. Y. Ma, S. Dai, S. Z. Qiao, *Mater. Today* **2016**, 19, 265.
- [115] a) S. Du, Z. Ren, J. Wu, W. Xi, H. Fu, *Nano Res.* **2016**, 9, 2260; b) T. Y. Ma, J. Ran, S. Dai, M. Jaroniec, S. Z. Qiao, *Angew. Chem., Int. Ed.* **2015**, 54, 4646.
- [116] Y. Xu, Y. Zhang, Z. Guo, J. Ren, Y. Wang, H. Peng, *Angew. Chem., Int. Ed.* **2015**, 54, 15390.
- [117] J. Fu, F. M. Hassan, J. Li, D. U. Lee, A. R. Ghannoum, G. Lui, M. A. Hoque, Z. Chen, *Adv. Mater.* **2016**, 28, 6421.
- [118] J. Fu, D. U. Lee, F. M. Hassan, L. Yang, Z. Bai, M. G. Park, Z. Chen, *Adv. Mater.* **2015**, 27, 5617.
- [119] J. Pan, Y. Y. Xu, H. Yang, Z. Dong, H. Liu, B. Y. Xia, *Adv. Sci.* **2018**, 5, 1700691.
- [120] a) H. Luo, W.-J. Jiang, Y. Zhang, S. Niu, T. Tang, L.-B. Huang, Y.-Y. Chen, Z. Wei, J.-S. Hu, *Carbon* **2018**, 128, 97; b) S. S. Shinde, J.-Y. Yu, J.-W. Song, Y.-H. Nam, D.-H. Kim, J.-H. Lee, *Nanoscale Horiz.* **2017**, 2, 333.
- [121] K. Gong, F. Du, Z. Xia, M. Durstock, L. Dai, *Science* **2009**, 323, 760.
- [122] S. Zhu, Z. Chen, B. Li, D. Higgins, H. Wang, H. Li, Z. Chen, *Electrochim. Acta* **2011**, 56, 5080.
- [123] H. W. Liang, X. Zhuang, S. Bruller, X. Feng, K. Mullen, *Nat. Commun.* **2014**, 5, 4973.
- [124] J. Ma, Z. Xiang, J. Zhang, *Sci. China: Chem.* **2018**, 61, 592.
- [125] D. Higgins, Z. Chen, D. U. Lee, Z. Chen, *J. Mater. Chem. A* **2013**, 1, 2639.
- [126] G. S. Park, J.-S. Lee, S. T. Kim, S. Park, J. Cho, *J. Power Sources* **2013**, 243, 267.
- [127] M. Wu, Y. Wang, Z. Wei, L. Wang, M. Zhuo, J. Zhang, X. Han, J. Ma, *J. Mater. Chem. A* **2018**, 6, 10918.
- [128] L. Wang, Y. Wang, M. Wu, Z. Wei, C. Cui, M. Mao, J. Zhang, X. Han, Q. Liu, J. Ma, *Small* **2018**, 14, 1800737.
- [129] L. Yang, S. Jiang, Y. Zhao, L. Zhu, S. Chen, X. Wang, Q. Wu, J. Ma, Y. Ma, Z. Hu, *Angew. Chem., Int. Ed.* **2011**, 50, 7132.
- [130] J. Liu, R. Wang, Z. Chen, N. Hu, C. Xu, Z. Shen, *ChemElectroChem* **2018**, 5, 1.
- [131] J. Zhang, H. Li, P. Guo, H. Ma, X. S. Zhao, *J. Mater. Chem. A* **2016**, 4, 8497.
- [132] L. Hadidi, E. Davari, M. Iqbal, T. K. Purkait, D. G. Ivey, J. G. Veinot, *Nanoscale* **2015**, 7, 20547.
- [133] a) M. Bockelmann, U. Kunz, T. Turek, *Electrochem. Commun.* **2016**, 69, 24; b) X. Liu, M. Park, M. G. Kim, S. Gupta, X. Wang, G. Wu, J. Cho, *Nano Energy* **2016**, 20, 315; c) S. W. T. Price, S. J. Thompson, X. Li, S. F. Gorman, D. Pletcher, A. E. Russell, F. C. Walsh, R. G. A. Wills, *J. Power Sources* **2014**, 259, 43.
- [134] Y. Qian, Z. Hu, X. Ge, S. Yang, Y. Peng, Z. Kang, Z. Liu, J. Y. Lee, D. Zhao, *Carbon* **2017**, 111, 641.
- [135] J. Zhang, L. Dai, *Angew. Chem., Int. Ed.* **2016**, 55, 13296.
- [136] S. S. Shinde, C. H. Lee, A. Sami, D. H. Kim, S. U. Lee, J. H. Lee, *ACS Nano* **2017**, 11, 347.
- [137] Y. Li, M. Gong, Y. Liang, J. Feng, J. E. Kim, H. Wang, G. Hong, B. Zhang, H. Dai, *Nat. Commun.* **2013**, 4, 1805.
- [138] P. Tan, B. Chen, H. Xu, H. Zhang, W. Cai, M. Ni, M. Liu, Z. Shao, *Energy Environ. Sci.* **2017**, 10, 2056.
- [139] Q. Liu, Z. Chang, Z. Li, X. Zhang, *Small Methods* **2018**, 2, 1700231.
- [140] X. Zhu, H. Yang, Y. Cao, X. Ai, *Electrochim. Acta* **2004**, 49, 2533.
- [141] J. Fu, J. Zhang, X. Song, H. Zarrin, X. Tian, J. Qiao, L. Rasen, K. Li, Z. Chen, *Energy Environ. Sci.* **2016**, 9, 663.
- [142] G. Li, X. Wang, J. Fu, J. Li, M. G. Park, Y. Zhang, G. Lui, Z. Chen, *Angew. Chem., Int. Ed.* **2016**, 55, 4977.
- [143] S. S. Shinde, C. H. Lee, J. Y. Yu, D. H. Kim, S. U. Lee, J. H. Lee, *ACS Nano* **2018**, 12, 596.
- [144] a) J. W. Choi, D. Aurbach, *Nat. Rev. Mater.* **2016**, 1, 16013; b) P. G. Bruce, S. A. Freunberger, L. J. Hardwick, J.-M. Tarascon, *Nat. Mater.* **2011**, 11, 19; c) Y. Tu, D. Deng, X. Bao, *J. Energy Chem.* **2016**, 25, 957.
- [145] a) H.-D. Lim, B. Lee, Y. Bae, H. Park, Y. Ko, H. Kim, J. Kim, K. Kang, *Chem. Soc. Rev.* **2017**, 46, 2873; b) Z. Lyu, Y. Zhou, W. Dai, X. Cui, M. Lai, L. Wang, F. Huo, W. Huang, Z. Hu, W. Chen, *Chem. Soc. Rev.* **2017**, 46, 6046.
- [146] J. Xie, X. Yao, Q. Cheng, I. P. Madden, P. Dornath, C.-C. Chang, W. Fan, D. Wang, *Angew. Chem., Int. Ed.* **2015**, 54, 1.
- [147] Z. Guo, D. Zhou, X. Dong, Z. Qiu, Y. Wang, Y. Xia, *Adv. Mater.* **2013**, 25, 5668.
- [148] J. Shui, F. Du, C. Xue, Q. Li, L. Dai, *ACS Nano* **2014**, 8, 3015.
- [149] Y. Lin, B. Moitoso, C. Martinez-Martinez, E. D. Walsh, S. D. Lacey, J. W. Kim, L. M. Dai, L. B. Hu, J. W. Connell, *Nano Lett.* **2017**, 17, 3252.